


 Cite this: *RSC Adv.*, 2025, 15, 42009

# Antimicrobial magnetic *Glycyrrhiza glabra* nanocomposite for decolouration of water through adsorption and photodegradation

 Ankita Manchanda,<sup>a</sup> Ahmed Hussain Jawhari,<sup>b</sup> Ziaul Hasan,<sup>c</sup> Nazim Hasan,<sup>bd</sup> Sneha Shukla,<sup>a</sup> Adiba Khan,<sup>a</sup> Tabrez Alam Khan<sup>a</sup> and Saif Ali Chaudhry<sup>\*a</sup>

A sustainable hybrid magnetic nanocomposite based on *Glycyrrhiza glabra* (GG), GG/ $\gamma$ -Fe<sub>2</sub>O<sub>3</sub>, was synthesized via one-pot co-precipitation method, and efficiently utilized for adsorption and photocatalytic degradation of two toxic model dyes, Congo red (CR) and Nile blue (NB) dyes from water. The characterization of the GG/ $\gamma$ -Fe<sub>2</sub>O<sub>3</sub> was performed by using FT-IR, P-XRD, BET-BJH, FE-SEM-EDX, TEM, SAED, XPS, TGA, UV-visible, and PL techniques. The GG/ $\gamma$ -Fe<sub>2</sub>O<sub>3</sub> showed significant inhibition of bacterial and fungal growth. The inhibition statistics towards gram-(+) and gram-(−) bacteria, and fungal strains were found superior as compared to the naive plant material. The influence of adsorption parameters, on dye removal efficiency, was appraised via batch methodology. The fitting of isothermal and kinetic datasets into their respective models indicated that the adsorptive removal process was governed by the Freundlich isotherm and pseudo-second order kinetics. The Langmuir saturation capacity for CR and NB was found to be 47.50 and 15.36 mg g<sup>−1</sup>, respectively. The spontaneous and physical sorption of CR and NB was delineated to be exothermic and endothermic, respectively, from 30 to 50 °C. The band gap of the GG/ $\gamma$ -Fe<sub>2</sub>O<sub>3</sub> were found 1.69 eV (indirect), and 2.30 eV (direct) which established its semiconducting design, with CR solar-degradation efficiency of 92.7%, following pseudo-first-order kinetics. The degradation intermediates and mechanism have been investigated from radical quenching experiments and high-resolution LC-MS. The GG/ $\gamma$ -Fe<sub>2</sub>O<sub>3</sub> exhibited structural integrity and excellent regeneration, supported by post-treatment FT-IR analysis. The reproducibility of the optimum experimental dataset under realistic conditions, including real wastewater, co-existing ions, and dye mixtures, revealed potent application of multifunctional and cost-effective GG/ $\gamma$ -Fe<sub>2</sub>O<sub>3</sub> for the efficient removal of both cationic and anionic water contaminants, as well as for reducing microbial loads.

 Received 12th July 2025  
 Accepted 4th October 2025

DOI: 10.1039/d5ra04982b

[rsc.li/rsc-advances](http://rsc.li/rsc-advances)

## 1 Introduction

The increasing level of water pollution, owing to industrialization and agricultural expansion, is of grave environmental concern.<sup>1</sup> Untreated or partially-treated aqueous wastewater, from various industries, is interspersed with mainstream water resources, which is detrimental to human life and aquatic organisms. Dyes are a significant class of recalcitrant toxic water contaminants emanating alongside various pigments and by-products from many industries.<sup>2</sup> From over 11 800 commercially available dyes/pigments, the annual global consumption is estimated at around 19 million metric tons. Textile (42.6%),

paint and coating (27.8%), plastic (16.3%), and paper, cosmetics and ink (13.3%) industries are the major consumers of dyes.<sup>3</sup> Around 10–15% industrial dyes are released into the environment during manufacturing and processing operations.<sup>4</sup> Congo red, CR, a highly water-soluble anionic diazo dye is utilized in textile, paper, plastic, and printing industries.<sup>5</sup> It is considered mutagenic, teratogenic, genotoxic, neurotoxic, cytotoxic, cutaneous, and carcinogenic.<sup>2,6</sup> The short-term ingestion of CR can lead to skin, eye, gastrointestinal irritation, and possible blood clotting.<sup>7</sup> Likewise, Nile blue, NB, is a cationic azine dye that finds application in the textile industry for dyeing cotton, wool, and other fabrics.<sup>8,9</sup> It can cause sleepiness, stimulation of the digestive tract, chills, respiratory tract allergy, redness, dryness/irritation of eyes/mouth/throat/skin, dermatitis, lung cancer, and even chromosomal aberrations.<sup>8,10,11</sup> The natural decomposition of such types of dyes is extremely difficult mainly due to their persistency, non-biodegradability, hydrophilicity, and stability.<sup>12,13</sup> Additionally, dyes alter water transparency, impede sunlight penetration into the water bodies, fluctuate the water quality parameters, and

<sup>a</sup>Department of Chemistry, Jamia Millia Islamia, New Delhi 110025, India. E-mail: schaudhry@jmi.ac.in

<sup>b</sup>Department of Physical Sciences, Chemistry Division, College of Science, Jazan University, P. O. Box 114, Jazan 45142, Saudi Arabia

<sup>c</sup>Department of Biosciences, Jamia Millia Islamia, New Delhi 110025, India

<sup>d</sup>Nanotechnology Research Unit, Jazan University, P.O. Box 114, Jazan 45142, Saudi Arabia


cumulate the oxidative stress, which in turn severely affects the aquatic biota owing to decreased photosynthetic action.<sup>14</sup> It is thereby imperative to amputate water resources of these hazardous pollutants, rendering water safe for human consumption.

Numerous techniques have been employed to clean dye-polluted water.<sup>15</sup> However, the conventional treatment methods are cumbersome, expensive, time and energy-consuming, show low removal efficiency and residual discharge.<sup>16</sup> Adsorption and photocatalytic degradation, of pollutants, have caught attention of many researchers, being simple, environment-friendly alternative, with minimum sludge formation, and high mineralization efficiency.<sup>17</sup>

Over last few decades, a variety of materials have been developed for the adsorptive removal of toxic dyes which include nanogels,<sup>18,19</sup> metal-oxide nanocomposites,<sup>20–23</sup> metal-organic frameworks,<sup>24</sup> plant-based materials,<sup>10,25</sup> and activated carbon/biochar<sup>26,27</sup> because of their ease of preparation, inexpensiveness, effectiveness over a wide range of pollutants, and porous structure with high adsorption capabilities and kinetics. However, restricted functionality, regeneration, and imitation to real environmental scenarios amidst competing conditions limit their practical application. Moreover, the complete removal of some azo-dyes (*e.g.*, CR) is rather difficult because of their complex aromatic structure, thermodynamic stability and non-biodegradability.<sup>11</sup> The secondary by-products formed being more toxic than the parent materials, render the synthesis of novel visible-light responsive photocatalysts and porous nanocomposites inevitable.<sup>28</sup>

Therefore, adsorption coupled with heterogeneous photocatalysis has received considerable attention as an economical, rapid and reliable treatment option. Many nanostructured metal oxides, preferably iron oxides such as magnetite ( $\text{Fe}_3\text{O}_4$ ) and maghemite ( $\gamma\text{-Fe}_2\text{O}_3$ )<sup>6,29–31</sup> and their hybrid nanocomposites<sup>13,32</sup> have evinced considerable interest for the removal of pernicious dyes, owing to surface defects, high surface area to volume ratio, intrinsic reactivity of surface functional sites, wide light response range, narrow band gap, chemical stability, low-cost, non-toxicity, biocompatibility, and abundance. Further, the surface modification of nanoparticles by compositing with plant residues (biomass) substantially reduces their strong tendency to agglomerate. Compositing also prevents premature surface saturation during treatment and acts as a solid-phase co-substrate to support oxide nanoparticles.<sup>33,34</sup> Additionally, the presence of pathogens, like bacteria and fungi, in wastewater, may cause severe health hazards, leading to various chronic and acute respiratory, gastrointestinal, and skin-related disorders.<sup>35</sup> Therefore, in addition to synergistic dye adsorption and photodegradation, the antipathogenic activity of the synthesized composite is vital to reduce the microbial loads of the polluted water.<sup>36–38</sup> *Glycyrrhiza glabra* (GG), commonly called licorice, is a traditional medicinal plant, possess therapeutic and pharmacological activities,<sup>39</sup> and is a proficient bio-sorptive material because of its active oxygenous functional surface sites.<sup>40</sup> It is a naturally abundant, biodegradable, and renewable bioresource, particularly, valued for its rich phytochemical composition, which bequeath antimicrobial and antioxidant potential.<sup>39</sup> The amalgamation of GG and  $\gamma\text{-Fe}_2\text{O}_3$  into a hybrid composite enhances

removal efficiency, surface active sites, structural stability, and recovery using magnetic separation to efficaciously treat wastewater for charged contaminants, and even microbes. It is a step forward towards circular bioeconomy, repurposing waste plant/agro-biomass to enhance resource efficiency, and minimize ecological impact to synthetic chemicals, promoting sustainable environmental remediation.<sup>41</sup> Moreover, research indicates use of iron oxide nanoparticles, particularly  $\text{Fe}_2\text{O}_3$  as iron micronutrient fertilizer for improved soil texture and plant growth. It gradually increases the level of iron in soil over time.<sup>42,43</sup> Thus, water enriched with GG and  $\gamma\text{-Fe}_2\text{O}_3$  together can enhance soil and water dynamics after treatment.

Several synthetic strategies, including green synthesis, hydrothermal, microemulsions, sol-gel, thermal decomposition, and co-precipitation, have been developed for the production of  $\gamma\text{-Fe}_2\text{O}_3$ -based nanocomposites.<sup>33</sup> Of these, co-precipitation is simplest, most cost-efficient, allows for better control of size and morphology, composition, stability, reproducibility, functionality, and can produce a large amount of product in a single batch.<sup>44</sup>

*G. glabra* (biomass and biochar) has been previously explored for water remediation,<sup>45–48</sup> however, much attempts have not been made towards its modification into nanocomposite. Moreover, no study has schematically delved into the multifunctional approach considering adsorption, photodegradation, and antimicrobial tendency of GG composites in real wastewater conditions.

Altogether, the present study outlines co-precipitation mediated synthesis of an inexpensive advanced multifunctional magnetic hybrid nanocomposite, GG/ $\gamma\text{-Fe}_2\text{O}_3$ , which was characterized using FT-IR, P-XRD, BET-BJH, FE-SEM-EDX, TEM, SAED, XPS, TGA, UV-visible, and PL techniques. The GG/ $\gamma\text{-Fe}_2\text{O}_3$  was explored for investigating its potential to decolourize wastewater by removing model CR and NB dyes. Different operational conditions (dosage, initial dye concentration, contact time, initial water pH and temperature) have been optimized. The sorption data was fitted into various isotherm and kinetic models, and thermodynamic equations for proposing plausible mechanism. The adsorption and degradation performance of the GG/ $\gamma\text{-Fe}_2\text{O}_3$  towards real wastewater, and in presence of competing ions, and dye mixtures have been thoroughly investigated. The stability, and regeneration potential have also been investigated. Lastly, the antibacterial and antifungal activities of the naive GG and GG/ $\gamma\text{-Fe}_2\text{O}_3$  against Gram-negative, *E. coli* (ATCC-25922), and Gram-positive, *S. aureus* (MTCC-902), bacterial strains, and fungal stain, *C. albicans* (SC-5314 and ATCC-90028), have also been investigated.

## 2 Materials and methods

### 2.1. Reagents and materials

The chemicals and instruments used for the synthesis and characterization of GG/ $\gamma\text{-Fe}_2\text{O}_3$  have been depicted in Tables S1 and S2, respectively.

### 2.2. Preparation of GG/ $\gamma\text{-Fe}_2\text{O}_3$

The GG roots were washed several times with deionized water to leach out solid or water-soluble impurities, oven-dried, and subjected to physical pre-treatment through



pulverization and sieving to a variable grain diameter (mesh) size of 60–200. Such pre-treatment downsizes particle dimensions and increases the available specific surface area<sup>49</sup> for the growth of  $\gamma$ - $\text{Fe}_2\text{O}_3$  nanoparticles on powdered GG following a slightly modified simple one-pot coprecipitation method.<sup>50,51</sup> 1.0 g of GG powder was dispersed in 100 mL of distilled water (DW) and ultrasonicated for 15 min to prepare a homogeneous suspension. The suspension was stirred, over a magnetic stirrer, followed by the addition of 100 mL of 0.5 M  $\text{Fe}(\text{NO}_3)_3 \cdot 9\text{H}_2\text{O}$  and 0.25 M  $\text{FeSO}_4 \cdot 7\text{H}_2\text{O}$  each, and was subjected to continuous stirring for 30 min at 50–60 °C. This was followed by the addition of 2 M NaOH solution dropwise until the suspension turned alkaline (~10–11 pH). The obtained brownish-black precipitate was allowed to settle, collected using a magnetic-separation method, and washed with deionized water, multiple times, followed by ethanol. It was oven-dried at 70 °C, calcined at 200 °C for 2 h, sieved, and stored in glass bottle. The schematic representation of the synthesis of GG/ $\gamma$ - $\text{Fe}_2\text{O}_3$  is depicted in Scheme 1.

### 2.3. Point of zero charge (ZPC)

The ZPC, pH at which the surface possesses zero charge,<sup>52</sup> was determined by following a slightly modified salt addition method.<sup>53</sup> A brief setup of a series of 100 mL Erlenmeyer flasks comprising double of the optimized dosage of GG/ $\gamma$ - $\text{Fe}_2\text{O}_3$  in 20 mL of 0.2 M  $\text{KNO}_3$  solutions, having pH variation in the pH range 2–10 were prepared and agitated for 24 h at 200 rpm. The final pHs of all solutions were recorded, and the point of intersection of the initial and final pHs curves established  $\text{pH}_{\text{ZPC}}$  of the GG/ $\gamma$ - $\text{Fe}_2\text{O}_3$ .

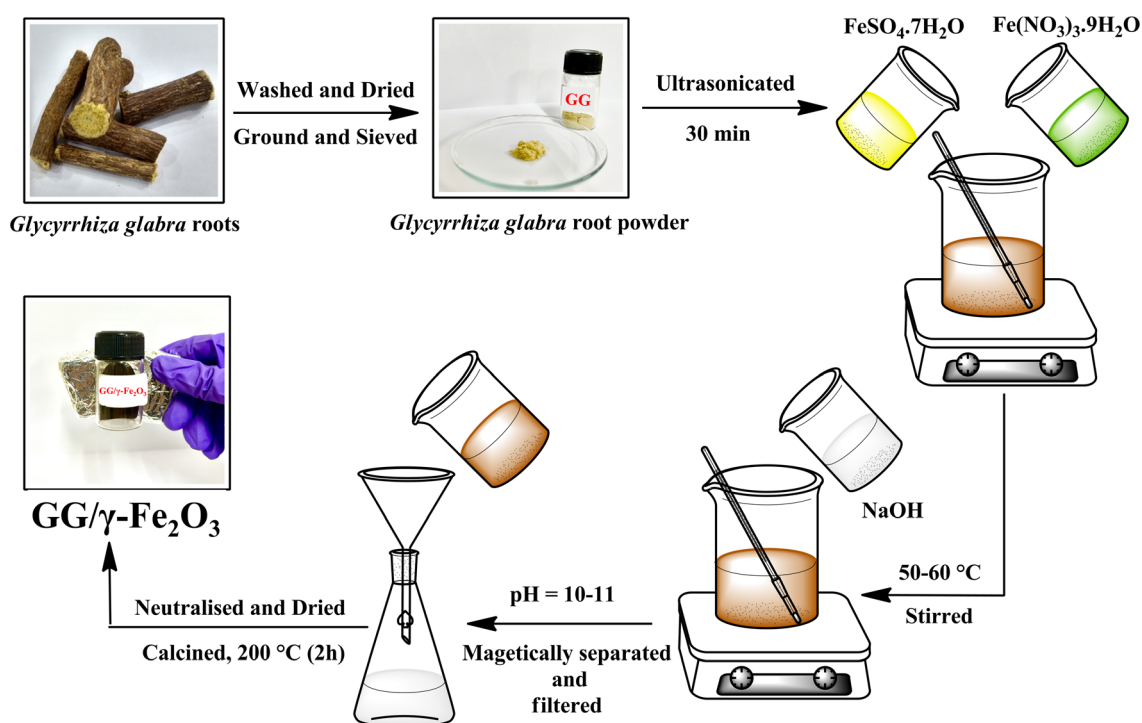
### 2.4. Antimicrobial activity

The antibacterial activities of the GG and GG/ $\gamma$ - $\text{Fe}_2\text{O}_3$  were investigated using *in vitro* 96-well microtiter assays against *E. coli* and *S. aureus* bacteria. The broth micro dilution method was followed for the determination of the minimum inhibitory concentration (MIC), and minimum bactericidal concentration (MBC).<sup>54</sup> Each test strain was cultivated overnight in nutrient broth, with the turbidity adjusted to 0.5 McFarland units in 100  $\mu\text{L}$  of Mueller–Hinton broth. The GG and GG/ $\gamma$ - $\text{Fe}_2\text{O}_3$  stock suspensions (5.0 mg  $\text{mL}^{-1}$ ) were added to each well. Positive and negative controls were also added, and then the plates were incubated at 37 °C for 12 h. To obtain MBC values, 100  $\mu\text{L}$  of turbidity-free tube content was cultured in Mueller–Hinton agar and incubated for 24 h at  $37 \pm 0.1$  °C.<sup>55</sup>

The antifungal efficacy of the GG and GG/ $\gamma$ - $\text{Fe}_2\text{O}_3$ , in terms of MIC and minimum fungicidal concentration (MFC)<sup>56</sup> were determined against *C. albicans* (SC-5314) and *C. albicans* (ATCC-90028), as described in the literature.<sup>57</sup> Briefly, 100  $\mu\text{L}$  of yeast peptone dextrose media (YPD) and GG and GG/ $\gamma$ - $\text{Fe}_2\text{O}_3$  stock solutions (5 mg  $\text{mL}^{-1}$ ) were added to the first well, which was then serially diluted. Following the addition of 100  $\mu\text{L}$  of fungal inoculant as a suspension in each well, the plates were incubated at 28 °C for 24 h. Plates without GG and GG/ $\gamma$ - $\text{Fe}_2\text{O}_3$  served as a negative control, while the antifungal drug, fluconazole, as a positive control. For both assays, the respective culture growth was noted as absorbance at 600 nm on Elisa plate reader. All experiments were conducted in triplicate simultaneously.

### 2.5. Batch adsorption study and statistical data analysis

The factors which affect the removal efficiency were optimized by varying GG/ $\gamma$ - $\text{Fe}_2\text{O}_3$  dosage (0.5–3 g  $\text{L}^{-1}$ ), dyes concentration



Scheme 1 Stepwise depiction of the synthesis of GG/ $\gamma$ - $\text{Fe}_2\text{O}_3$  nanocomposite.



(5–30 mg L<sup>-1</sup>), reaction time (15–120 min), solution pH (2–11), and temperature (30, 40, 50 °C). Briefly, in 100 mL Erlenmeyer flasks, CR and NB solutions (10 mL) having concentrations of 10 and 20 mg L<sup>-1</sup>, respectively, were mechanically shaken at 200 rpm at 30 °C and natural pH with varying dosage for 120 min. The effect of temperature was investigated using the optimized dosage of GG/γ-Fe<sub>2</sub>O<sub>3</sub> (2.0 g L<sup>-1</sup>), and [CR] = 10 mg L<sup>-1</sup> and [NB] = 20 mg L<sup>-1</sup>. The experiments were performed in triplicate, and the mean values have been reported.

The rationale for selecting the experimental variables and their transferability to real systems was supported by preliminary batch adsorption trials and relevant literature.<sup>53,58</sup> The initial screening experiments, using 0.5–3 g L<sup>-1</sup> GG/γ-Fe<sub>2</sub>O<sub>3</sub> for 5–30 mg L<sup>-1</sup> CR and NB, showed good adsorption results without causing saturation or particle agglomeration. The time of contact, 15–120 min, ensured sufficient sorbent–pollutant interactions and practical treatment duration, as evident from the kinetic investigation. The pH range 2–11 was chosen, considering the pH sensitivity of CR and NB dyes, to obtain the maximum adsorption. Further, the reproducibility, reliability, and statistical significance of the experimentally optimized variables were realized using one-way analysis of variance (ANOVA, Origin Pro 8.5), at the 0.05 level. The standard deviation (SD) values (Table S3) have been depicted as error in Fig. S3, while the complete statistical analysis is given in Table S4. The realized experimental variable range ensured an efficient sorptive system and statistically valid optimisation.

After adsorption and magnetic separation of the dye-loaded GG/γ-Fe<sub>2</sub>O<sub>3</sub>, the concentrations of residual dyes were determined at λ<sub>max</sub> 498 nm for CR and 627 nm for NB using a UV-visible spectrophotometer (T80+ UV/VIS, PG instruments Ltd, Leicestershire, England). The following equations were employed for the evaluation of per cent removal [eqn (1)] and equilibrium adsorption capacity [eqn (2)] of the GG/γ-Fe<sub>2</sub>O<sub>3</sub>.<sup>59</sup>

$$\text{Removal efficiency (\% removal)} = \frac{(C_0 - C_e)}{C_0} \times 100 \quad (1)$$

$$Q_e = (C_0 - C_e) \times \frac{V}{m} \quad (\text{mass balance relationship}) \quad (2)$$

where, *m* (g) is the mass of GG/γ-Fe<sub>2</sub>O<sub>3</sub>, *V* (L) is volume of CR or NB solution; *C*<sub>0</sub> and *C*<sub>e</sub> are initial and final equilibrium concentrations of the dye solutions (mg L<sup>-1</sup>), respectively; and *Q*<sub>e</sub> (mg g<sup>-1</sup>) is the equilibrium adsorption capacity of the GG/γ-Fe<sub>2</sub>O<sub>3</sub>.

## 2.6. Photocatalytic degradation

Photocatalytic activity of the GG/γ-Fe<sub>2</sub>O<sub>3</sub> against CR was investigated at its optimized sorption conditions. 2.0 g L<sup>-1</sup> of nanocomposite was placed in 100 mL of 10 mg L<sup>-1</sup> CR solution in dark for 1 h, under constant stirring for attainment of adsorption–desorption equilibrium on the catalytic surface. It was followed by subsequent irradiation under sunlight with uninterrupted stirring for 0–160 min. 10 mL of the degraded supernatant dye solution was withdrawn at 20 min intervals, centrifuged, and analysed spectrophotometrically. The time-dependent UV-visible spectra (*A* vs. *λ*) were recorded from *λ*

250 to 600 nm, for different intervals of time, and photocatalytic degradation efficiency (% DE) was evaluated using the following equation<sup>60</sup> [eqn (3)]:

$$\begin{aligned} \text{Photocatalytic degradation efficiency (\% DE)} \\ = \frac{(C_0 - C_t)}{C_0} \times 100 \end{aligned} \quad (3)$$

where, *C*<sub>*t*</sub> (mg L<sup>-1</sup>) is the concentration of the dye solution at irradiation time *t*.

The kinetics of the degradation, and the rate constant of the process were computed by employing the following pseudo-first order kinetic relationship [eqn (4)]:

$$\ln\left(\frac{C_t}{C_0}\right) = \ln\left(\frac{A_t}{A_0}\right) = -kt \quad (4)$$

where, *k* is the pseudo-first order rate constant, while *A*<sub>0</sub>/*C*<sub>0</sub> and *A*<sub>*t*</sub>/*C*<sub>*t*</sub> are the initial and final absorbance/concentration, respectively.<sup>60</sup>

Further, radical trapping experiments were performed for the detection of active degradation species.<sup>61</sup> 4.0 mL each of benzoquinone (BQ, 1 mM), isopropanol (IPA, 2:20 vol/vol), and ethylenediaminetetraacetic acid (EDTA, 10 mM) scavengers were introduced to 100 mL, 10 mg L<sup>-1</sup> CR solution, and used to trap superoxide radicals (O<sub>2</sub><sup>-•</sup>), hydroxyl radicals (OH<sup>•</sup>), and holes (h<sup>+</sup>), respectively. Lastly, a plausible mechanism, for the photodegradation of CR, has been proposed in accordance with the liquid chromatography-high resolution mass spectrometry (LC-HRMS) results.

## 2.7. Real wastewater analysis and effect of co-existing ions

The adsorption and photodegradation tendency of GG/γ-Fe<sub>2</sub>O<sub>3</sub> towards actual real water sample were evaluated using sewage water (SW, collected from sewage treatment plant, Batla House, New Delhi), RO water (RO), and tap water (TW) spiked with 10 mg L<sup>-1</sup> CR and 20 mg L<sup>-1</sup> NB dye concentrations, under optimized conditions, at their natural pH. Such water samples have ample co-existing ions which might compete with the charged organic water contaminants for sorptive sites, interfering with their removal. Thereby, 10 mM of various inorganic anions (Cl<sup>-</sup>, NO<sub>3</sub><sup>-</sup>, SO<sub>4</sub><sup>2-</sup>, and CO<sub>3</sub><sup>2-</sup>), and cations (Na<sup>+</sup>, Ca<sup>2+</sup>) were selected to investigate the adsorption and degradation effect of GG/γ-Fe<sub>2</sub>O<sub>3</sub> for CR and NB.

## 2.8. Adsorption selectivity in dye mixture

Real wastewater might contain a mixture of organic dyes, and the advancement of new materials for targeted adsorption relies on their selectivity. The adsorption selectivity of 2.0 g L<sup>-1</sup> GG/γ-Fe<sub>2</sub>O<sub>3</sub> for CR and NB dyes was justified through single-dye system, their binary mixture, and of their mixture in a quaternary setup of two anionic (A) and two cationic (C) dyes each. The concentrations of all anionic dyes were taken as 10 mg L<sup>-1</sup>, and cationic dyes as 20 mg L<sup>-1</sup>.

## 2.9. Regeneration study

The reusability analysis of the spent GG/γ-Fe<sub>2</sub>O<sub>3</sub> is significant for commercial application to diminish the overall treatment

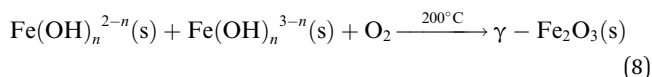
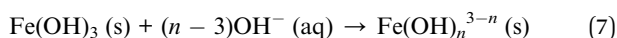
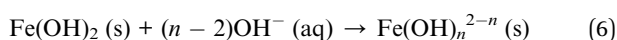
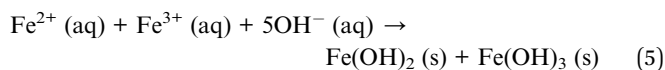


cost, promoting a sustainable and efficient water treatment process. For regeneration, 2.0 g L<sup>-1</sup> of CR/NB-loaded GG/ $\gamma$ -Fe<sub>2</sub>O<sub>3</sub> nanocomposite was dispersed in 10 mL of ethanol and the suspensions were agitated in a water bath shaker at 30 °C at 200 rpm for 4 h. The spent GG/ $\gamma$ -Fe<sub>2</sub>O<sub>3</sub> was washed until neutral pH, dried, and subjected to subsequent reusability–regeneration cycles. The percentage removal of dyes were determined spectrophotometrically in each cycle using eqn (1). The stability of spent GG/ $\gamma$ -Fe<sub>2</sub>O<sub>3</sub> was established *via* FT-IR analysis post adsorption of CR and NB after a considerable number of adsorption–desorption cycles.

### 3 Result and discussion

#### 3.1. Mechanism for preparation of GG/ $\gamma$ -Fe<sub>2</sub>O<sub>3</sub>

The mechanism of formation of GG/ $\gamma$ -Fe<sub>2</sub>O<sub>3</sub> can be understood by considering the entrapment of Fe<sup>2+</sup> and Fe<sup>3+</sup> by oxygeneous groups (–OH and –COOH) at the GG surface through site-specific adsorption. The precipitating agent NaOH supplies enough OH<sup>-</sup> which might have electrostatically attracted the adsorbed Fe<sup>2+</sup> and Fe<sup>3+</sup> yielding respective hydroxides, M(OH)<sub>x</sub> that ultimately transformed into multiple hydroxyls bearing Fe(OH)<sub>n</sub><sup>2-n</sup> and Fe(OH)<sub>n</sub><sup>3-n</sup> species.<sup>62</sup> Afterwards, dehydration and subsequent nucleation of these hydroxides, on porous GG surface, might have led to the formation of  $\gamma$ -Fe<sub>2</sub>O<sub>3</sub>, and later GG/ $\gamma$ -Fe<sub>2</sub>O<sub>3</sub> *via* incorporation with the GG framework (Fig. S1). However, it may also be stated that the high concentration of NaOH, in the reaction mixture, might have also been responsible for driving the nucleation process towards the formation of tiny nuclei, leading to a decrease in the crystallite size of particles.<sup>63</sup> A theoretical mechanism depicting the formation of GG/ $\gamma$ -Fe<sub>2</sub>O<sub>3</sub> can be proposed as [eqn (5)–(9)]:<sup>62,64,65</sup>



#### 3.2. Characterization

**3.2.1. Fourier transform infrared spectroscopy.** The Fourier transform infrared (FT-IR) analysis of the GG root powder specified the chemical composition and bonding of various functional groups, which results in the formation of the GG/ $\gamma$ -Fe<sub>2</sub>O<sub>3</sub>. The FT-IR spectrum of the GG {Fig. 1A(a)} showed a large number of peaks in the range 4000–650 cm<sup>-1</sup>. A broad band, for O–H bonds due to alcoholic/phenolic compounds, like cellulose, hemicellulose or lignin, owing to intermolecular hydrogen bonding, was observed at 3362 cm<sup>-1</sup>. It was followed by strong anti-symmetric and medium symmetric C–H stretching

frequencies of aliphatic –CH<sub>3</sub> and –CH<sub>2</sub> groups around 2930 and 2882 cm<sup>-1</sup>, respectively.<sup>66</sup> The absorption peaks around 2136, 1637, and 1516 cm<sup>-1</sup> corresponded to the presence of benzene rings of flavonoids, phytosterols, *etc.*, appeared for stretching vibrations of C≡C, C=O in polyphenol carbonyl or carboxyl groups of flavonoids in conjugation with, or of C=C of aliphatic and aromatic systems.<sup>66,67</sup> Moreover, the peak at 1637 cm<sup>-1</sup> also depicted the bending vibration of the O–H bond due to the entrapped moisture.<sup>68</sup> The peaks at 1423 and 1370 cm<sup>-1</sup> indicated the C–H bending vibrations due to –CH<sub>3</sub> and –CH<sub>2</sub> groups, respectively, from aliphatic chains or methoxy (O–CH<sub>3</sub>) groups in lignocellulosic materials. The bands at 1246, 1152, and 1026 cm<sup>-1</sup> explicated deformational vibration of the C–O bond from acids, and/or ester functional groups of glycosides.<sup>66,69</sup> While, the presence of flavonoids and saponins were confirmed by strong coupled vibrations at 849 and 762 cm<sup>-1</sup> due to out-of-plane bending deformations of C–H bond.<sup>66</sup> Thereby, the abundance of alcoholic, phenolic, carbonyl, carboxyl, and ester functional groups, on the GG surface, was quite evident.

The FT-IR spectrum of the GG/ $\gamma$ -Fe<sub>2</sub>O<sub>3</sub> {Fig. 1A(b)} was scrutinized to discern the nature of interactions between GG surface functional groups and the integrated oxides. Slightly shifted and less intense peaks, with usual annotations to GG, were ascertained at 3378, 2925, 2854, 1624, 1462, 1381, 1022, 887, and 794 cm<sup>-1</sup>. The peak at 1152 cm<sup>-1</sup> showed no shifting; however, some of the minor peaks got quenched, and some new peaks were spotted. This behaviour could be attributed to the possible increase in bond strength and formation of electrostatic and hydrogen bonds. Some new peaks, in the range 650–400 cm<sup>-1</sup>, depicted the successful formation of GG/ $\gamma$ -Fe<sub>2</sub>O<sub>3</sub> *via* metal–oxygen bond vibrations. Peaks at 623, 589, and 449 cm<sup>-1</sup> might be attributed to the Fe–O–C stretching vibrations which are characteristics of  $\nu$ (Fe–O) stretching mode in iron oxides.<sup>68,70</sup>

**3.2.2. Powder-X-ray diffraction crystallography.** The Powder-X-ray diffraction (P-XRD) patterns of GG and GG/ $\gamma$ -Fe<sub>2</sub>O<sub>3</sub> (Fig. 1B) were analyzed in the angular range 5–90° (2 $\theta$ ). A broad peak around 22.48° (2 $\theta$ ) was observed for the GG corresponding to the (002) plane, characteristic peak of amorphous cellulosic material.<sup>71</sup> However, the diffraction pattern of the GG/ $\gamma$ -Fe<sub>2</sub>O<sub>3</sub> manifested distinct intense peaks at 18.14° (111), 30.1° (220), 35.54° (311), 43.46° (400), 53.98° (422), 57.16° (511), 62.76° (440), 70.9° (620), 73.98° (533), 78.86° (622) 21.14° (200), 23.78° (210), 26.10° (211), 32.24° (300), and 39.36° (320) due to the presence of  $\gamma$ -Fe<sub>2</sub>O<sub>3</sub> (JCPDS PDF-04-0755). Moreover, a gradual change in colour from black to brownish black on heating exemplified the slow oxidation of magnetite to maghemite.<sup>72</sup> The angular values ruled out the possibility of formation of other types of iron oxides, *i.e.*, hematite ( $\alpha$ -Fe<sub>2</sub>O<sub>3</sub>), goethite [FeO(OH)], wüstite (FeO), *etc.*<sup>73</sup> Meanwhile, the occurrence of most intense peak at 35.54°, corresponding to (311) plane, was close to the standard angular value of 35.597° for  $\gamma$ -Fe<sub>2</sub>O<sub>3</sub>, signifying  $\gamma$ -Fe<sub>2</sub>O<sub>3</sub> as the predominant crystalline phase in GG/ $\gamma$ -Fe<sub>2</sub>O<sub>3</sub>.<sup>22</sup> On comparison of the two diffractograms (Fig. 1B) it was observed that GG/ $\gamma$ -Fe<sub>2</sub>O<sub>3</sub> displayed peaks of both GG and  $\gamma$ -Fe<sub>2</sub>O<sub>3</sub> at various 2 $\theta$  levels. However, the intensity of diffraction peak at 22.48° for GG significantly got reduced in



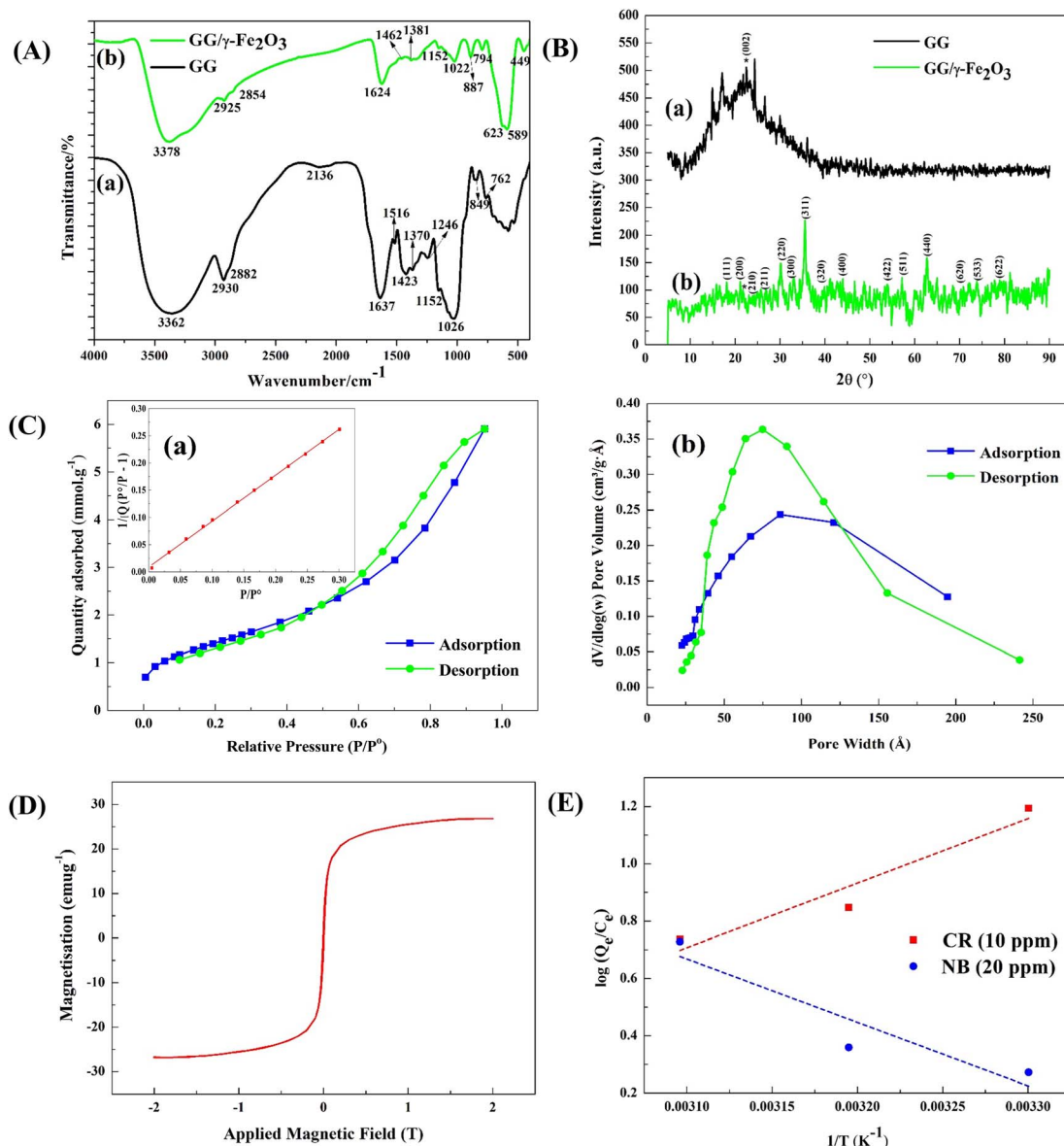


Fig. 1 (A) FT-IR spectra of (a) GG, and (b) GG/ $\gamma$ -Fe<sub>2</sub>O<sub>3</sub>; (B) P-XRD analysis of (a) GG, and (b) GG/ $\gamma$ -Fe<sub>2</sub>O<sub>3</sub>; (C) (a) BET, and (b) BJH curves; (D)  $M$ - $H$  magnetization curve of GG/ $\gamma$ -Fe<sub>2</sub>O<sub>3</sub>; (E) Van't Hoff plots.

GG/ $\gamma$ -Fe<sub>2</sub>O<sub>3</sub> owing to chemical interactions between its oxygenous functional groups and  $\gamma$ -Fe<sub>2</sub>O<sub>3</sub> nanoparticles. The mean crystallite size, corresponding to prominent peaks of the XRD pattern, was estimated by fitting the angular data in the Debye-Scherrer equation (eqn (S1))<sup>74</sup> as 36.09 nm, confirming the nanostructure of high surface area, suitable for greater dye adsorption. Moreover, the nature and intensity of the peaks indicated low crystallinity of GG/ $\gamma$ -Fe<sub>2</sub>O<sub>3</sub>.

**3.2.3. BET and BJH analysis.** Brunauer-Emmett-Teller (BET) and Barrett-Joyner-Halenda (BJH) analysis was followed to determine surface area, average pore width, and single point total pore volume (of pores less than 413.690 Å width at  $P/P^0 = 0.951$ ) of the GG/ $\gamma$ -Fe<sub>2</sub>O<sub>3</sub>, which were found to be 114.454 m<sup>2</sup> g<sup>-1</sup>, 71.549 Å, and 0.205 cm<sup>3</sup> g<sup>-1</sup>, respectively. The amount of the N<sub>2</sub> gas adsorbed by the GG/ $\gamma$ -Fe<sub>2</sub>O<sub>3</sub> decreased with reducing

pressure, and N<sub>2</sub> adsorption-desorption isotherm was similar to Type-IV, characteristic of a mesoporous structure {Fig. 1C(a)}.<sup>75</sup> The adsorption average pore size ( $4 V A^{-1}$ ) distribution was centered at 75.251 Å, while the desorption average pore size ( $4 V A^{-1}$ ) was found to be 70.258 Å from the BJH plot {Fig. 1C(b)}. The specific surface area and porosity of the GG/ $\gamma$ -Fe<sub>2</sub>O<sub>3</sub> were found to be appreciably high, indicating superior physical and textural characteristics.

**3.2.4. Vibrating sample magnetometry.** The magnetic hysteresis,  $M$ - $H$  curve, recorded *via* vibrating sample magnetometry (VSM), indicated the magnetic nature of the GG/ $\gamma$ -Fe<sub>2</sub>O<sub>3</sub> in field strength of -2 T to +2 T (Fig. 1D). An S-shaped curve was observed, which suggested superparamagnetism, at room temperature mainly of the single magnetic domains of the nanoparticles in the material.<sup>76</sup> The saturation magnetic



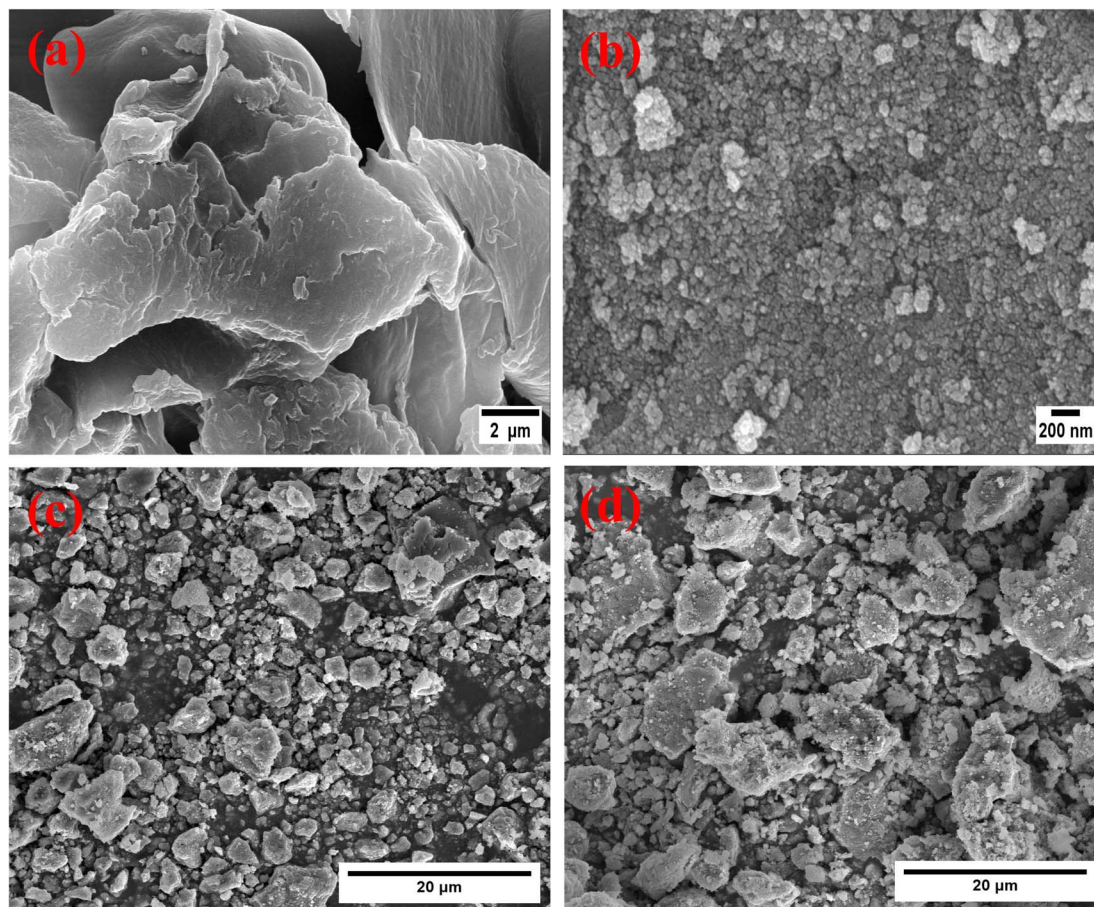


Fig. 2 FE-SEM images of (a) GG, (b) GG/ $\gamma$ -Fe<sub>2</sub>O<sub>3</sub>, (c) GG/ $\gamma$ -Fe<sub>2</sub>O<sub>3</sub> before adsorption, and (d) GG/ $\gamma$ -Fe<sub>2</sub>O<sub>3</sub>@CR.

moment,  $M_s$ , of the GG/ $\gamma$ -Fe<sub>2</sub>O<sub>3</sub> was found to be 26.827 emu g<sup>-1</sup>, which is modest for the easy magnetic separation of the nanocomposite from the treated water.

**3.2.5. FE-SEM-EDX and TEM.** Field emission scanning electron microscopy (FE-SEM) imaging revealed a smooth and even surface of GG (Fig. 2a) and the introduction of heterogeneity and roughness in the GG/ $\gamma$ -Fe<sub>2</sub>O<sub>3</sub> surface due to clustering of irregular oxide nanoparticles (Fig. 2b and c). An enhancement in overall contending porosity and surface area was observed in GG/ $\gamma$ -Fe<sub>2</sub>O<sub>3</sub> for increased CR and NB uptake. The CR accumulation on the GG/ $\gamma$ -Fe<sub>2</sub>O<sub>3</sub> surface (Fig. 2d) caused abatement of even surface with significant accretion making the surface inhomogeneous. Elemental composition of the GG and GG/ $\gamma$ -Fe<sub>2</sub>O<sub>3</sub> were ascertained from the energy dispersive X-ray spectroscopy, EDX, and elemental mapping (Fig. 3a and b). The normalized atomic percentage of 67.70% C, and 32.30% O were detected for GG, while the composition fluctuated to 23% C, 64% O, and 13% Fe owing to the nanostructured growth of  $\gamma$ -Fe<sub>2</sub>O<sub>3</sub> on GG framework. The analysis suggested the presence of C, H and O due to GG, while increase in % O, decrease in % C, and presence of iron was due to formation of nanostructured Fe(III) oxide which deposited in the form  $\gamma$ -Fe<sub>2</sub>O<sub>3</sub>.

Transmission electron microscopy (TEM) (Fig. 4a and c) provided a clear indication of the average size distribution of

the GG/ $\gamma$ -Fe<sub>2</sub>O<sub>3</sub> particles. The mean particle size of the GG/ $\gamma$ -Fe<sub>2</sub>O<sub>3</sub> (Fig. 4b) was estimated around 31.92 nm, which is in line with the XRD result (Fig. 1B). The contrast between the brighter GG framework and darker patches of  $\gamma$ -Fe<sub>2</sub>O<sub>3</sub> corresponded to the uniform deposition, entrapment, and random dispersion of nanoparticles throughout. Moreover, the TEM images confirmed the amorphous and heterogeneous nature of GG/ $\gamma$ -Fe<sub>2</sub>O<sub>3</sub>. The lattice fringes with protuberant electron diffraction rings in the selected area electron diffraction (SAED) pattern (Fig. 4d) indicated an amorphous nature with slight crystallinity of  $\gamma$ -Fe<sub>2</sub>O<sub>3</sub> nanoparticles in GG/ $\gamma$ -Fe<sub>2</sub>O<sub>3</sub>.<sup>77</sup> The  $d$ -spacing values and corresponding Miller indices of the six diffraction rings (Table S5) aligned with the XRD findings.

**3.2.6. X-ray photoelectron spectroscopy.** The chemical environment and the elemental valence states were further investigated through X-ray photoelectron spectroscopy (XPS) analysis of the GG/ $\gamma$ -Fe<sub>2</sub>O<sub>3</sub> (Fig. 5). The co-existence of elements Fe, O, and C was confirmed, which was consistent with the EDX data. The high-resolution narrow spectrum of Fe 2p (Fig. 5b) matches the core-level binding energies of the spin-orbit doublets Fe 2p<sub>3/2</sub> and Fe 2p<sub>1/2</sub>, centered at 710.4 and 724 eV, which is characteristic of Fe<sup>3+</sup> in  $\gamma$ -Fe<sub>2</sub>O<sub>3</sub>. The Fe<sup>3+</sup> 2p<sub>3/2</sub> can be deconvoluted into two distinct sub peaks at 710.2 and 712 eV for Fe<sup>3+</sup> in octahedral and tetrahedral sites, respectively.<sup>78</sup> Further,



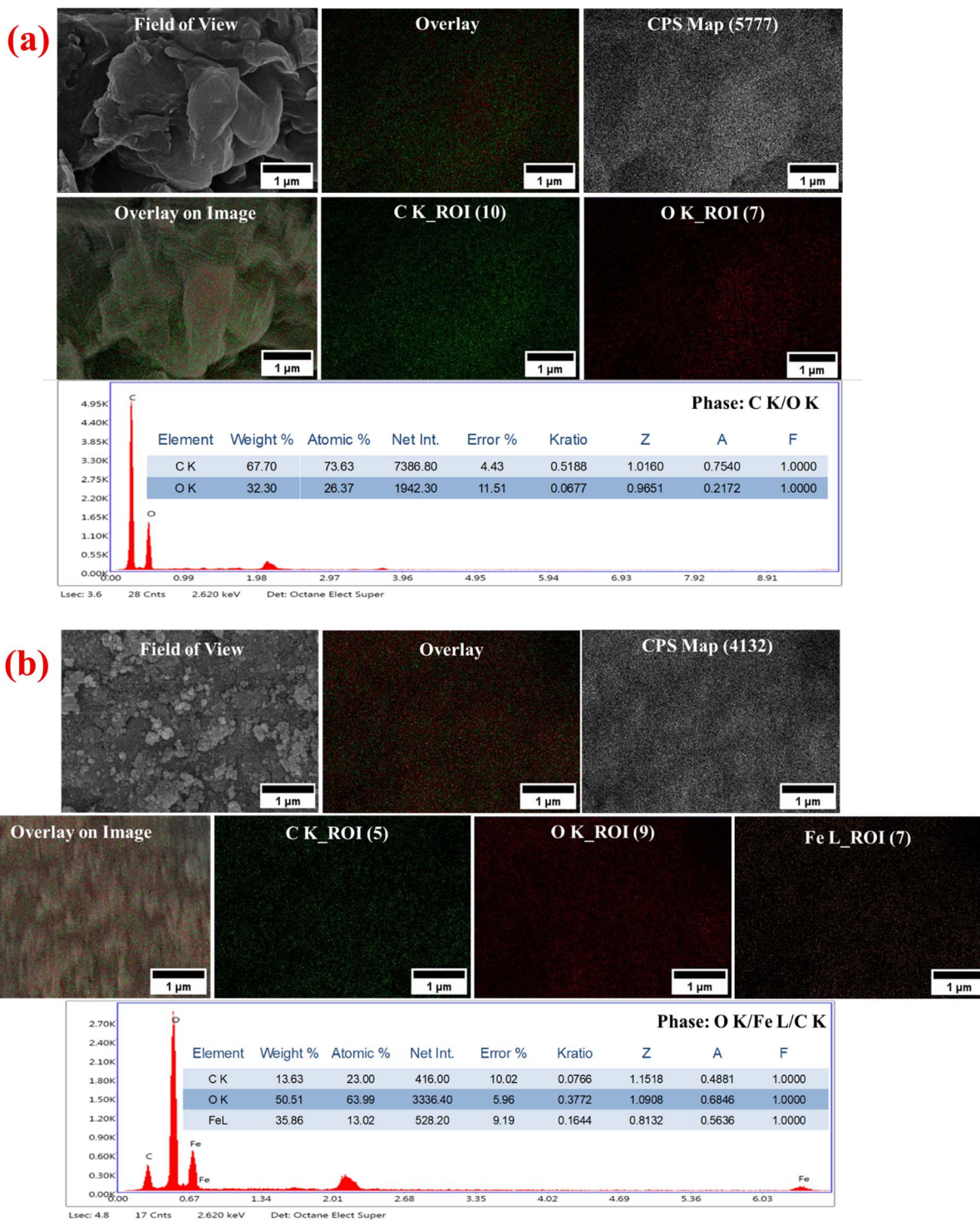


Fig. 3 EDX and mapping of (a) GG and (b) GG/ $\gamma$ -Fe<sub>2</sub>O<sub>3</sub>.

shake-up satellite peaks for Fe 2p<sub>3/2</sub> at 718.9, and Fe 2p<sub>1/2</sub> at 733<sup>79</sup> were indicative of transition of Fe-3d electrons to empty 4s orbital during ejection of core 2p photoelectrons.<sup>78</sup> Moreover, the O 1s scan of GG/ $\gamma$ -Fe<sub>2</sub>O<sub>3</sub> (Fig. 5c) validated the prevalence of Fe–O bonds *via* peak at binding energy 529.6 eV; and the peak at 531 eV was assigned to C–O–Fe bond linkage between GG carbon framework and  $\gamma$ -Fe<sub>2</sub>O<sub>3</sub>.<sup>80</sup> An additional peak at 532 eV

was attributed to the C–O units (C–OH/C–O–C) in oxygen-containing functional groups.<sup>81</sup> Lastly, the C 1s XPS spectrum (Fig. 5d) exhibited three fitted peaks of C–C/C=C, C–O, and O–C=O centered at 284.6, 286.18 and 288.2 eV.<sup>82</sup> These results validated the FT-IR established functional groups and the formation of new metal–oxygen bonding interactions in the GG/ $\gamma$ -Fe<sub>2</sub>O<sub>3</sub> nanocomposite.



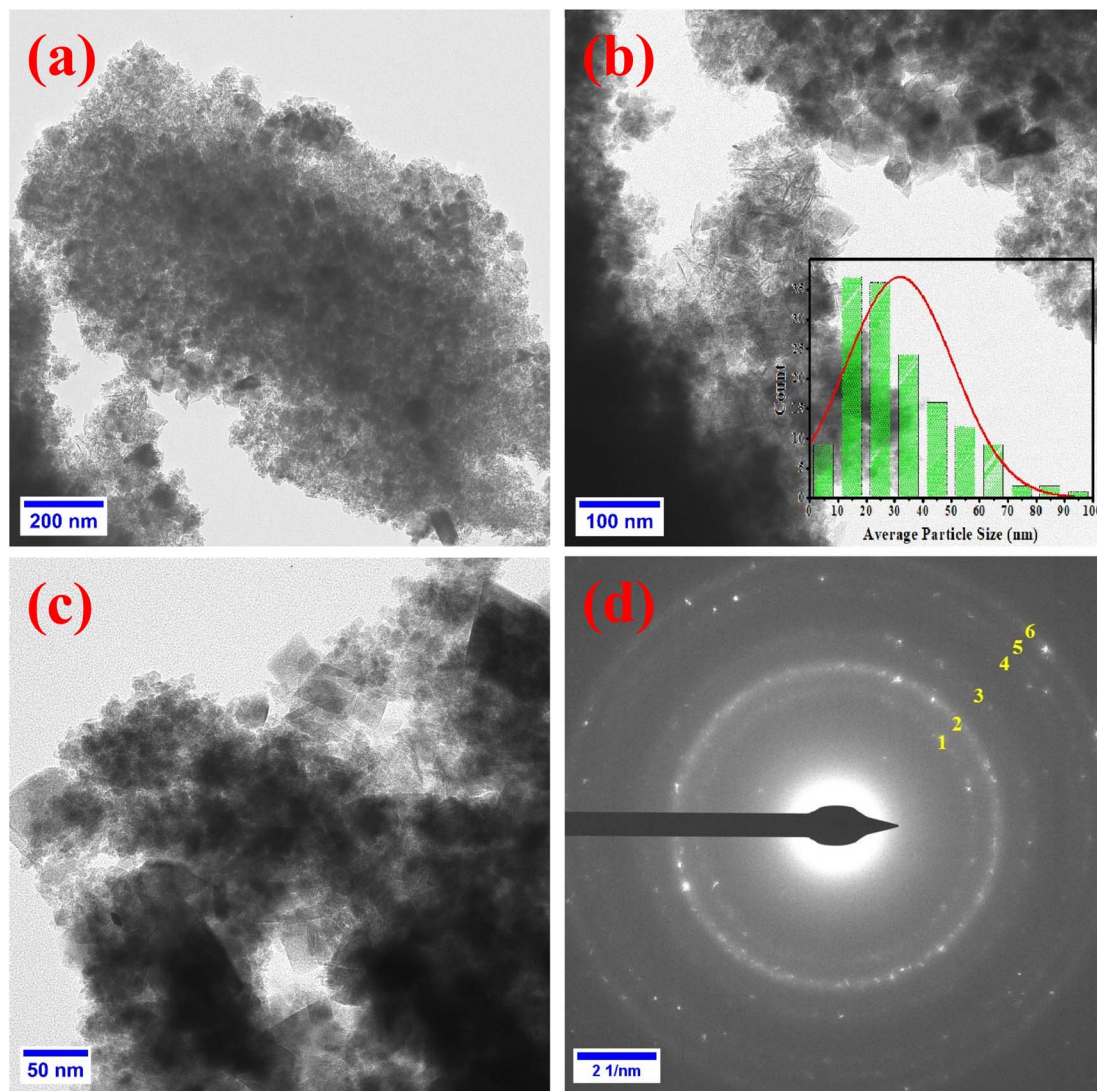


Fig. 4 (a)–(c) represent TEM images, and (d) the SAED ring pattern of GG/ $\gamma$ -Fe<sub>2</sub>O<sub>3</sub>.

**3.2.7. Thermogravimetric analysis (TGA).** The weight loss curve of the GG/ $\gamma$ -Fe<sub>2</sub>O<sub>3</sub>, due to thermal decomposition (Fig. 5e), shows gradual weight loss of 6.13% from room temperature to around 190 °C, related to the removal of residual surface water molecules. The primary decomposition of the sample occurred around 200–470 °C, accompanying biomass pyrolysis.<sup>83</sup> A slight weight change was observed at higher temperature, more than 470 °C due to phase transition.<sup>84</sup> The residual weight percent of 77.63% was realized, indicating high structural and thermal stability of the nanocomposite.

**3.2.8. Optical properties of GG/ $\gamma$ -Fe<sub>2</sub>O<sub>3</sub>.** The UV-visible spectroscopic analysis of the GG/ $\gamma$ -Fe<sub>2</sub>O<sub>3</sub> (Fig. S2a) showed peaks between 320–420 nm, which are typically associated with the surface plasmon resonance of iron in  $\gamma$ -Fe<sub>2</sub>O<sub>3</sub>.<sup>85</sup> The band gap energy,  $E_g$ , is crucial for predicting the photochemical and photophysical characteristics of material that is used for photocatalytic dye degradation.  $\gamma$ -Fe<sub>2</sub>O<sub>3</sub> based semiconductors have been known to exhibit both indirect [ $O^{2-}(2p) \rightarrow Fe^{3+}(3d)$ ] and direct [ $Fe^{3+}(3d) \rightarrow 3d$ ] transitions.<sup>86–88</sup> The indirect and

direct transition band gap of the GG/ $\gamma$ -Fe<sub>2</sub>O<sub>3</sub>, were determined by the Tauc plot, and found 1.69 and 2.30 eV, respectively (Fig. S2b and c). These band gap energy values established its semiconducting nature.

The photoluminescence (PL) spectra of the GG (Fig. S2d), GG/ $\gamma$ -Fe<sub>2</sub>O<sub>3</sub> and pure  $\gamma$ -Fe<sub>2</sub>O<sub>3</sub> (Fig. 5f) were acquired at an excitation wavelength of 325 nm to comprehend the charge carrier separation efficiency and the recombination rate of electron–hole pair. The emission varied from 350 to 800 nm, with broad and intense emission bands centered at  $\sim$ 480 nm and  $\sim$ 565 nm in pure  $\gamma$ -Fe<sub>2</sub>O<sub>3</sub> nanoparticles which might be due to exciton emission, and radiative recombination of mobile and trapped electrons on octahedral and tetrahedral sites of  $\gamma$ -Fe<sub>2</sub>O<sub>3</sub>, respectively.<sup>89</sup> However, the intensity of the peaks reduced significantly in GG/ $\gamma$ -Fe<sub>2</sub>O<sub>3</sub>, confirming the hampering of recombination of photogenerated charge carriers. The PL spectra of GG was of highest intensity, which reduced drastically on combination with  $\gamma$ -Fe<sub>2</sub>O<sub>3</sub>.



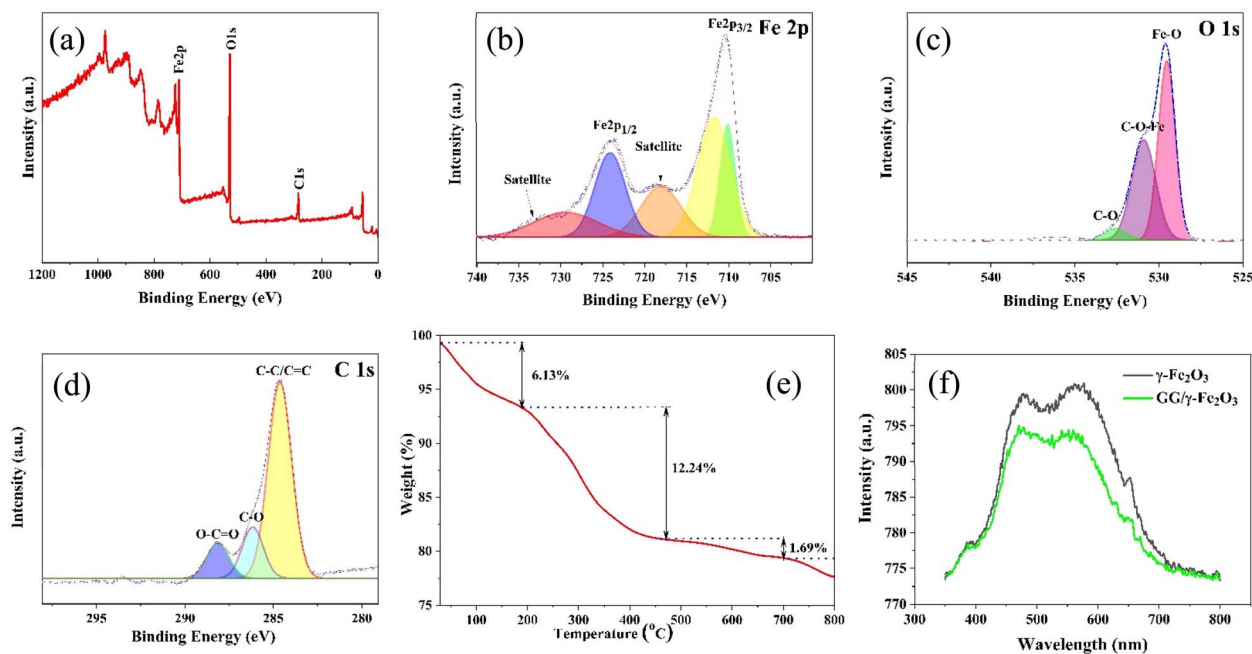


Fig. 5 (a) The full survey scan, and high-resolution spectra of (b) Fe 2p, (c) O 1s, (d) C 1s of GG/γ-Fe<sub>2</sub>O<sub>3</sub>; (e) TGA of GG/γ-Fe<sub>2</sub>O<sub>3</sub>; (f) PL spectra of γ-Fe<sub>2</sub>O<sub>3</sub> and GG/γ-Fe<sub>2</sub>O<sub>3</sub>.

### 3.3. Inhibition of growth of microorganisms

The GG and GG/γ-Fe<sub>2</sub>O<sub>3</sub> exhibited dose-dependent inhibition of pathogenic bacteria. The MICs of GG were found to be 550.25 ± 1.85 and 425.5 ± 1.25 μg mL<sup>-1</sup>, whereas for GG/γ-Fe<sub>2</sub>O<sub>3</sub>, these values were found to be 250 ± 3.15 and 200 ± 2.62 μg mL<sup>-1</sup>, for *E. coli* and *S. aureus*, respectively (Table S6). The lower MIC values of the GG/γ-Fe<sub>2</sub>O<sub>3</sub> against both Gram-negative and Gram-positive bacteria, in comparison to GG, suggested the superiority of GG/γ-Fe<sub>2</sub>O<sub>3</sub> for treating bacterial pathogens in wastewater. The GG and GG/γ-Fe<sub>2</sub>O<sub>3</sub> generally showed more antibacterial effects against Gram-positive bacteria, due to differences in cell composition and thickness, compared to Gram-negative bacteria. The findings were aligned with previous studies that also indicated the antimicrobial potential of the GG.<sup>90,91</sup>

In addition, the GG and GG/γ-Fe<sub>2</sub>O<sub>3</sub> also exhibited significant antifungal activity against two *Candida albicans* strains. The GG exhibited MICs of 300.85 ± 8.58 μg mL<sup>-1</sup> and 320.74 ± 5.65 μg mL<sup>-1</sup>, while GG/γ-Fe<sub>2</sub>O<sub>3</sub> showed MICs of 131.25 ± 2.56 μg mL<sup>-1</sup> and 125 ± 1.15 μg mL<sup>-1</sup>, for *C. albicans* (SC5314) and *C. albicans* (ATCC90028), respectively, and separately (Table S7). The lower MIC and MFC values of the GG/γ-Fe<sub>2</sub>O<sub>3</sub> indicated a more efficient and potent antifungal nature. Thereby, it could be justified that the enhanced antibacterial and antifungal activity of the GG/γ-Fe<sub>2</sub>O<sub>3</sub> could be attributed to the combined effect of phytochemical contents in GG and iron oxide nanoparticles, which might have diffused and interacted with the bacterial and fungal lipid layer within their cell membrane.<sup>92</sup>

### 3.4. CR and NB sorption investigation

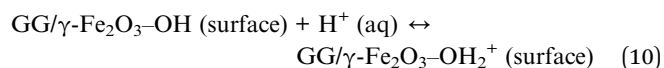
**3.4.1. Influence of operational parameters on the dye removal efficiency of GG/γ-Fe<sub>2</sub>O<sub>3</sub>.** At first, with increase of GG/γ-

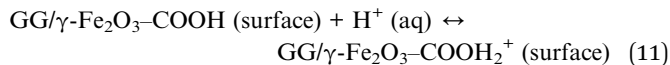
Fe<sub>2</sub>O<sub>3</sub> dose, from 0.5 to 2.0 g L<sup>-1</sup>, a relative increase in adsorption of CR, from 68.58 to 90.49%, and NB, from 68.92 to 95.90%, was observed (Fig. S3a). The observation could be justified due to the enhancement of the overall specific surface area of GG/γ-Fe<sub>2</sub>O<sub>3</sub>, which is highly porous in nature. The FT-IR spectrum confirmed the presence of oxygenous adsorptive sites on the GG/γ-Fe<sub>2</sub>O<sub>3</sub> surface which increased up to 2.0 g L<sup>-1</sup> for both dyes. Following, at higher doses, the reduction in the amount of CR and NB against largely available adsorption active sites saturated the surface.<sup>22,93</sup>

2.0 g L<sup>-1</sup> of the GG/γ-Fe<sub>2</sub>O<sub>3</sub> efficaciously removed around 97% CR from 10 mg L<sup>-1</sup> solution and 79% NB from the 20 mg L<sup>-1</sup> solution. At higher concentrations, the percentage adsorption reduced slightly to 96% and 72% for 30 mg L<sup>-1</sup> CR and NB, respectively (Fig. S3b). This observation could be attributed to the saturation of the available active sites on the otherwise fixed amount of GG/γ-Fe<sub>2</sub>O<sub>3</sub>, which prevented further adsorption. Thus, as low as 10 mg L<sup>-1</sup> CR and 20 mg L<sup>-1</sup> NB concentrations were optimized, since the released dye concentration in industrial effluent is not too high.

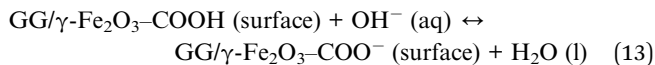
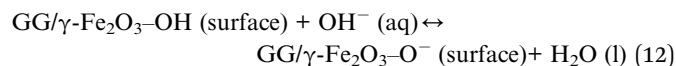
pH of water influence electrostatic interactions, directs the surface charge of solid, and the extent of ionization of dyes in water.<sup>94</sup> Numerous surface functional sites (-COOH, -OH) are subjected to modification, *i.e.*, either through protonation or deprotonation at pH below and above ZPC, bestowing either positive (-COOH<sub>2</sub><sup>+</sup>, -OH<sub>2</sub><sup>+</sup>) or negative (-COO<sup>-</sup>, -O<sup>-</sup>) charge to the surface, respectively, as depicted below [eqn (10)–(13)]:

At acidic pH





At alkaline pH



The GG/ $\gamma$ -Fe<sub>2</sub>O<sub>3</sub> showed higher uptake capacity for CR in acidic medium, however, an insignificant gradual decrease in percentage sorption was observed on transition to neutral conditions, which further steepened in alkaline environment, *i.e.*, 59.07% at pH = 11.<sup>95</sup> Moreover, NB removal was at its lowest (40.36%) in highly acidic conditions (pH = 2) and increased significantly from pH 4 to 8. The maximum adsorption of NB onto GG/ $\gamma$ -Fe<sub>2</sub>O<sub>3</sub> was obtained at pH 11 (Fig. S3c).

The sorption trend of GG/ $\gamma$ -Fe<sub>2</sub>O<sub>3</sub> can be explained on the basis of the ZPC of 6.9, indicating a nearly amphoteric surface (Fig. S4). In acidic pH (pH < ZPC), the GG/ $\gamma$ -Fe<sub>2</sub>O<sub>3</sub> exhibited greater CR adsorption owing to extensive electrostatic interactions between the protonated positively charged GG/ $\gamma$ -Fe<sub>2</sub>O<sub>3</sub> surface and negatively charged CR ions. Additionally, around pH 8, hydrogen bonding between surface functional groups of the GG/ $\gamma$ -Fe<sub>2</sub>O<sub>3</sub> and -NH<sub>2</sub> group in CR was majorly governing its uptake.<sup>22</sup> Conversely, at higher pH, the coulombic repulsion between the negatively charged deprotonated surface and the anionic CR relinquished its uptake.

Reversibly, the cationic NB exhibited favourable sorption at higher pH (pH > ZPC) following deprotonation of the GG/ $\gamma$ -Fe<sub>2</sub>O<sub>3</sub> surface by OH<sup>-</sup>, bestowing negative charge to the surface. Moreover, the extensive protonation of the GG/ $\gamma$ -Fe<sub>2</sub>O<sub>3</sub> at low pH (pH < ZPC) decreased the sorption of positively charged NB. Further, there might be a sense of competition between H<sup>+</sup>/H<sub>3</sub>O<sup>+</sup> and NB ions for binding sites at low pH, resulting in slower NB sorption. Therefore, a combination of electrostatic and hydrogen bonding interactions might be responsible for the adsorptive removal of CR and NB by GG/ $\gamma$ -Fe<sub>2</sub>O<sub>3</sub>.

Monitoring of contact time, for 10 mg L<sup>-1</sup> CR and 20 mg L<sup>-1</sup> NB sorption onto 2.0 g L<sup>-1</sup> GG/ $\gamma$ -Fe<sub>2</sub>O<sub>3</sub>, elucidated a continuous increment in the percentage adsorption with increasing time (Fig. S3d). The adsorption of CR and NB by GG/ $\gamma$ -Fe<sub>2</sub>O<sub>3</sub> proceeded in two phases: an instantaneous initial fast phase, followed by a later slow phase. The rate of removal of CR and NB showed a steady increase till 60 min (optimum time), removing nearly 88% CR and 93% NB within the first 15 min, increasing gradually to 94% CR and 96% NB removal at 60 min, after which the transport rate diminished, and nearly became constant for a prolonged time of contact. The trend can be explained based on of the availability of abundant vacant active sites (with COO<sup>-</sup> and OH<sup>-</sup> groups) initially, providing an easy pathway for interaction between dye molecules and 2.0 g L<sup>-1</sup> GG/ $\gamma$ -Fe<sub>2</sub>O<sub>3</sub>. With time, the need for specific pathways subjugated the adsorption rate onto the partially available or later filled sites, attaining equilibrium.<sup>96</sup>

**3.4.2. Effect of temperature and thermodynamics.** The CR removal by the GG/ $\gamma$ -Fe<sub>2</sub>O<sub>3</sub> decreased with increasing temperature, which can be attributed to an increase in mobility and a decrease in diffusion rates of CR into pores.<sup>97</sup> Furthermore, with an increase in temperature, the weakly-bonded CR ions might have escaped from their binding sites in response to bond breakage. For instance, weak hydrogen bonds are susceptible to breakage upon receiving energy at 40 and 50 °C, resulting in reduced adsorption capacity at higher temperatures.<sup>98</sup> Thereby, CR adsorption onto GG/ $\gamma$ -Fe<sub>2</sub>O<sub>3</sub> surface was exothermic in nature.<sup>99</sup> On the other hand, NB adsorption showed an increase with the rise in temperature, indicating an endothermic process.<sup>100</sup> The activation of GG/ $\gamma$ -Fe<sub>2</sub>O<sub>3</sub> surface at high temperatures made the adsorptive sites readily available for NB sorption.<sup>97</sup>

Adsorption thermodynamics was studied by appraising the changes in enthalpy ( $\Delta H$ ), entropy ( $\Delta S$ ), and Gibbs free energy ( $\Delta G$ ). Substituting the experimental data in thermodynamic equations (eqn (S2) and (S3))<sup>101,102</sup> delivered negative values of  $\Delta G$ , *i.e.*, -6.928, -5.076, and -4.552 kJ mol<sup>-1</sup> for 10 mg L<sup>-1</sup> CR, and -1.579, -2.151, and -4.501 kJ mol<sup>-1</sup> for 20 mg L<sup>-1</sup> NB sorption, at 30, 40, and 50 °C, respectively (Table 1). These values indicated the thermodynamic feasibility of CR and NB sorption onto GG/ $\gamma$ -Fe<sub>2</sub>O<sub>3</sub> within the tested temperature range. Besides,  $\Delta G$ , between 0 and -20 kJ mol<sup>-1</sup>, suggested physisorption of CR and NB dyes onto the surface of GG/ $\gamma$ -Fe<sub>2</sub>O<sub>3</sub>.<sup>103</sup> The surface charge significantly influences the thermodynamics of physical adsorption by altering the interaction energy, electrostatic interactions around ZPC, and strength of the weak bonding (van der Waals) interactions between the dye molecules and the interface, posing substantial impact on the overall extent of adsorption.<sup>104,105</sup> The balance between physisorption and electrostatic interactions drives the whole sorption process. The electrostatic attractions enhance physisorption and make  $\Delta G$  more negative, while electrostatic repulsions decrease physisorption and increase the  $\Delta G$  value. On increasing temperature, the order of  $\Delta G$  for CR removal became less negative, while a corresponding increase in negative value was observed for NB removal, suggesting a decrease in the adsorption rate in the former and a corresponding increase in the latter. For NB adsorption, a higher negative  $\Delta G$  at elevated temperatures indicated greater spontaneity and affinity due to electrostatic interactions between NB and GG/ $\gamma$ -Fe<sub>2</sub>O<sub>3</sub> at 50 °C. This indicated endothermic adsorption of NB which could be justified from the positive value of  $\Delta H$  (+42.408 kJ mol<sup>-1</sup>). Moreover, a positive  $\Delta S$  (+0.144 kJ mol<sup>-1</sup> K<sup>-1</sup>) value suggested good affinity of NB towards GG/ $\gamma$ -Fe<sub>2</sub>O<sub>3</sub>, and increased randomness at the dye-adsorbent interface (Table 1). Van't Hoff plot (Fig. 1E) produced negative  $\Delta H$ , -43.146 kJ mol<sup>-1</sup>, confirming exothermic thermodynamics for CR adsorption. Moreover, for CR sorption, the plot also showed a decrease in randomness,  $\Delta S$  = -0.120 kJ mol<sup>-1</sup> K<sup>-1</sup>, at the interface, indicating adsorption accompanied by a corresponding reduction in the degrees of freedom at the solid-liquid interface. It might be due to a probable increase in affinity between CR and GG/ $\gamma$ -Fe<sub>2</sub>O<sub>3</sub> surface through van der Waals, electrostatic and



Table 1 Non-linear isotherm and thermodynamic parameters for CR and NB adsorption onto GG/ $\gamma$ -Fe<sub>2</sub>O<sub>3</sub>

Parameter	CR			NB			
	30 °C	40 °C	50 °C	30 °C	40 °C	50 °C	
Langmuir isotherm $Q_e = \frac{Q_0 b C_e}{1 + b C_e}$	$Q_0$ (mg g <sup>-1</sup> )	39.744	39.789	47.504	15.361	14.902	13.305
	$b$ (L mg <sup>-1</sup> )	0.412	0.188	0.118	0.259	0.365	1.508
	$R_L$	0.195	0.347	0.459	0.162	0.120	0.032
	$R^2$	0.986	0.994	0.993	0.996	0.980	0.990
	$\chi^2$	0.284	0.113	0.112	0.036	0.221	0.142
Freundlich isotherm $Q_e = k_F C_e^{1/n}$	$k_F$ [(L mg <sup>-1</sup> ) <sup>1/n</sup> (mg g <sup>-1</sup> )]	11.455	6.261	5.092	3.544	4.313	7.063
	$1/n$	0.756	0.778	0.815	0.529	0.481	0.351
	$n$	1.323	1.286	1.227	1.892	2.077	2.845
	$R^2$	0.996	0.998	0.998	0.990	0.997	0.953
	$\chi^2$	0.082	0.029	0.039	0.099	0.037	0.653
Temkin isotherm $Q_e = \beta_T \ln(k_T C_e)$	$k_T$ (L mg <sup>-1</sup> )	11.712	4.559	3.453	3.002	5.633	17.264
	$b_T$ (kJ mol <sup>-1</sup> )	0.547	0.532	0.541	0.793	0.928	0.993
	$R^2$	0.891	0.925	0.921	0.981	0.950	0.997
	$\chi^2$	2.149	1.336	1.359	0.196	0.554	0.038
	$k_{D-R}$	0.628	1.452	2.019	3.004	2.552	0.474
D-R isotherm $Q_e = Q_{D-R} \exp \left[ -k_{D-R} \left( \ln \left( 1 + \frac{1}{C_e} \right) \right)^2 \right]$	$Q_{D-R}$ (mg g <sup>-1</sup> )	15.894	14.158	13.849	9.853	10.506	11.185
	$E_{D-R}$ (kJ mol <sup>-1</sup> )	2.248	1.527	1.336	1.028	1.152	2.758
	$R^2$	0.902	0.892	0.881	0.843	0.809	0.928
	$\chi^2$	1.931	1.926	2.031	1.607	2.130	0.993
	$\Delta G$ (kJ mol <sup>-1</sup> )	-6.928	-5.076	-4.552	-1.579	-2.151	-4.501
$\Delta H$ (kJ mol <sup>-1</sup> )		-43.146			+42.408		
$\Delta S$ (kJ mol <sup>-1</sup> K <sup>-1</sup> )		-0.120			+0.144		

hydrogen bonding interactions. However, the magnitude of  $\Delta H$ , less than 80 kJ mol<sup>-1</sup> for both CR and NB adsorption, supported weak physical interaction with GG/ $\gamma$ -Fe<sub>2</sub>O<sub>3</sub> surface.<sup>106</sup>

**3.4.3. Modelling of adsorption isotherms.** The sorption data, at 30, 40, and 50 °C for CR and NB (5–30 mg L<sup>-1</sup>), and 2.0 g L<sup>-1</sup> GG/ $\gamma$ -Fe<sub>2</sub>O<sub>3</sub>, were fitted into different isotherm models to decipher the corresponding isotherm parameters, which delineate the surface characteristics, interactions, and sorption capacity (Table 1). The non-linear regression analysis was conducted using OriginPro 8.5 software. The statistical treatment of experimental data concerning error analysis and conformity to various models was performed using correlation coefficient ( $R^2$ ) and reduced chi-square ( $\chi^2$ ), represented by eqn (14) and (15).

$$R^2 = \frac{\sum_{i=1}^N \left( Q_{e(\text{cal})} - \bar{Q}_{e(\text{meas})} \right)_i^2}{\sum_{i=1}^N \left[ \left( Q_{e(\text{cal})} - \bar{Q}_{e(\text{meas})} \right)_i^2 + \left( Q_{e(\text{cal})} - \bar{Q}_{e(\text{meas})} \right)_i^2 \right]} \quad (14)$$

$$\chi_{\text{red}}^2 = \frac{1}{N-p} \sum_{i=1}^N \left[ \frac{\left( Q_{e(\text{meas})} - Q_{e(\text{cal})} \right)^2}{Q_{e(\text{cal})}} \right]_i \quad (15)$$

where  $Q_{e(\text{cal})}$  and  $Q_{e(\text{meas})}$  are the calculated (theoretical) and measured (experimental) adsorption capacities (mg g<sup>-1</sup>), respectively,  $\bar{Q}_{e(\text{meas})}$  (mg g<sup>-1</sup>) is the average of  $Q_{e(\text{meas})}$ ,  $p$  represents the number of model parameters, and  $N$  is the number of experimental data points.

**3.4.3.1. Langmuir isotherm.** The Langmuir isotherm assumes homogeneous, one molecule per site, monolayer adsorption onto finite and degenerate adsorptive sites *via* physical or chemical forces, without lateral interactions.<sup>107</sup> Non-

linear Langmuir isotherm<sup>108</sup> expounded maximum adsorption capacities,  $Q_0$ , in the range 39.744–47.504 mg g<sup>-1</sup> for CR (increasing) and 15.361–13.305 mg g<sup>-1</sup> for NB (decreasing) sorption, representing endothermic and exothermic adsorption, respectively, within 30–50 °C. This observation deviated from the thermodynamic interpretations. Moreover, the corresponding values of Langmuir constant,  $b$ , representing the extent of affinity in terms of binding energy was determined from the non-linear Langmuir isotherm plots (Fig. S5a and b), which decreased from 0.412 to 0.118 L mg<sup>-1</sup> for CR; increased from 0.259 to 1.508 L mg<sup>-1</sup> for NB removal, suggesting lower heat of adsorption/affinity of CR, and higher heat of sorption/affinity of NB with increasing temperature, which was also not in accordance with  $\Delta S$  values. These interpretations suggested disagreement between the experimental data and the derived Langmuir parameters (Table 1).

In addition, the separation factor,  $R_L \left( = \frac{1}{(1 + bC_0)} \right)$ , specifies the shape of an isotherm and the reversibility of a process. If  $0 < R_L < 1$ , then the sorption is considered feasible and energetically favourable, whereas  $R_L = 0$  implies an irreversible adsorption phenomenon, and  $R_L = 1$  indicates linearity.<sup>109</sup>  $R_L$  values between 0 and 1 confirmed the energetically feasible adsorption of CR and NB onto the GG/ $\gamma$ -Fe<sub>2</sub>O<sub>3</sub> surface within the tested temperature range.

**3.4.3.2. Freundlich isotherm.** The Freundlich isotherm assumes surface as heterogeneous and physical adsorption onto energetically non-uniform sites with explicit bond energies, resulting in multilayers *via* lateral interactions. It considers an exponential decrease in sorption energy upon surface coverage.<sup>110</sup> Non-linear,  $Q_e$  vs.  $C_e$ , Freundlich plots, for



CR (Fig. 6a) and NB (Fig. 6b) adsorption onto GG/ $\gamma$ -Fe<sub>2</sub>O<sub>3</sub>, demonstrated best-fit statistics to the experimental sorption data, in terms of  $R^2$  nearest to unity. This extraction could be further confirmed from the texture of GG/ $\gamma$ -Fe<sub>2</sub>O<sub>3</sub> particles in the SEM micrographs (Fig. 2b) which indicated a heterogeneous multi-layer formation. The Freundlich parameter,  $k_F$ , decreased from 11.455 to 5.092 (L mg<sup>-1</sup>)<sup>1/n</sup> (mg g<sup>-1</sup>) for CR, and increased from 3.544 to 7.063 (L mg<sup>-1</sup>)<sup>1/n</sup> (mg g<sup>-1</sup>) for NB adsorption in the temperature range 30–50 °C, indicating low adsorption capacity for CR (exothermic), and high capacity for NB (endothermic) sorption at elevated temperatures. This conclusion was found in accordance with the thermodynamic data set, dictating the Freundlich isotherm fitting for both CR and NB dye removal data. The heterogeneity factor,  $n$ , obtained in the range 1–10 ( $n > 1$ ) and  $1 < 1/n < 0$  (Table 1), established favourable physical adsorption with strong interaction of CR/NB and the GG/ $\gamma$ -Fe<sub>2</sub>O<sub>3</sub> surface.<sup>110</sup>

**3.4.3.3. Temkin isotherm.** The Temkin isotherm considers heterogeneous solute–solid interactions. It assumes orderly distribution of binding energy to a certain extent, and linear decrease in adsorption enthalpy with surface coverage.<sup>111</sup> Non-linear plots of Temkin isotherm, for CR (Fig. S5c) and NB

(Fig. S5d) adsorption onto the GG/ $\gamma$ -Fe<sub>2</sub>O<sub>3</sub>, produced parameters  $k_T$  (L mg<sup>-1</sup>) and  $b_T$  (kJ mol<sup>-1</sup>), where  $b_T$  ( $=RT/\beta_T$ ) is associated with heat of adsorption, and  $\beta_T$  is the Temkin constant. The  $k_T$  corresponds to the maximum binding energy and is the binding constant. The respective decrease (from 11.712 to 3.453 L mg<sup>-1</sup>) and increase (from 3.002 to 17.264 L mg<sup>-1</sup>) in parameter  $k_T$ , from 30–50 °C, for CR and NB adsorption reinforced the exothermic and endothermic nature of the sorption processes, respectively. The considerable difference in  $k_T$  between 30 and 40 °C indicated significant variation in the binding capabilities for CR adsorption. Moreover, the closeness in  $b_T$  values for CR directed a similar extent of binding probability and constant sorption enthalpy at all temperatures. Conversely, for NB sorption, a notable increase in  $k_T$  was observed between 40 and 50 °C, indicating a change in bonding pattern. It can be stated that the reported typical range of bonding energy for ion exchange mechanism is between 8 and 16 kJ mol<sup>-1</sup>,<sup>112</sup> however, the observed low values ( $b_T < 8$  kJ mol<sup>-1</sup>) indicated weak van der Waals interactions between CR/NB and GG/ $\gamma$ -Fe<sub>2</sub>O<sub>3</sub>.

**3.4.3.4. Dubinin–Radushkevich isotherm.** The Dubinin–Radushkevich (D–R) isotherm illustrates pore-filling nature of

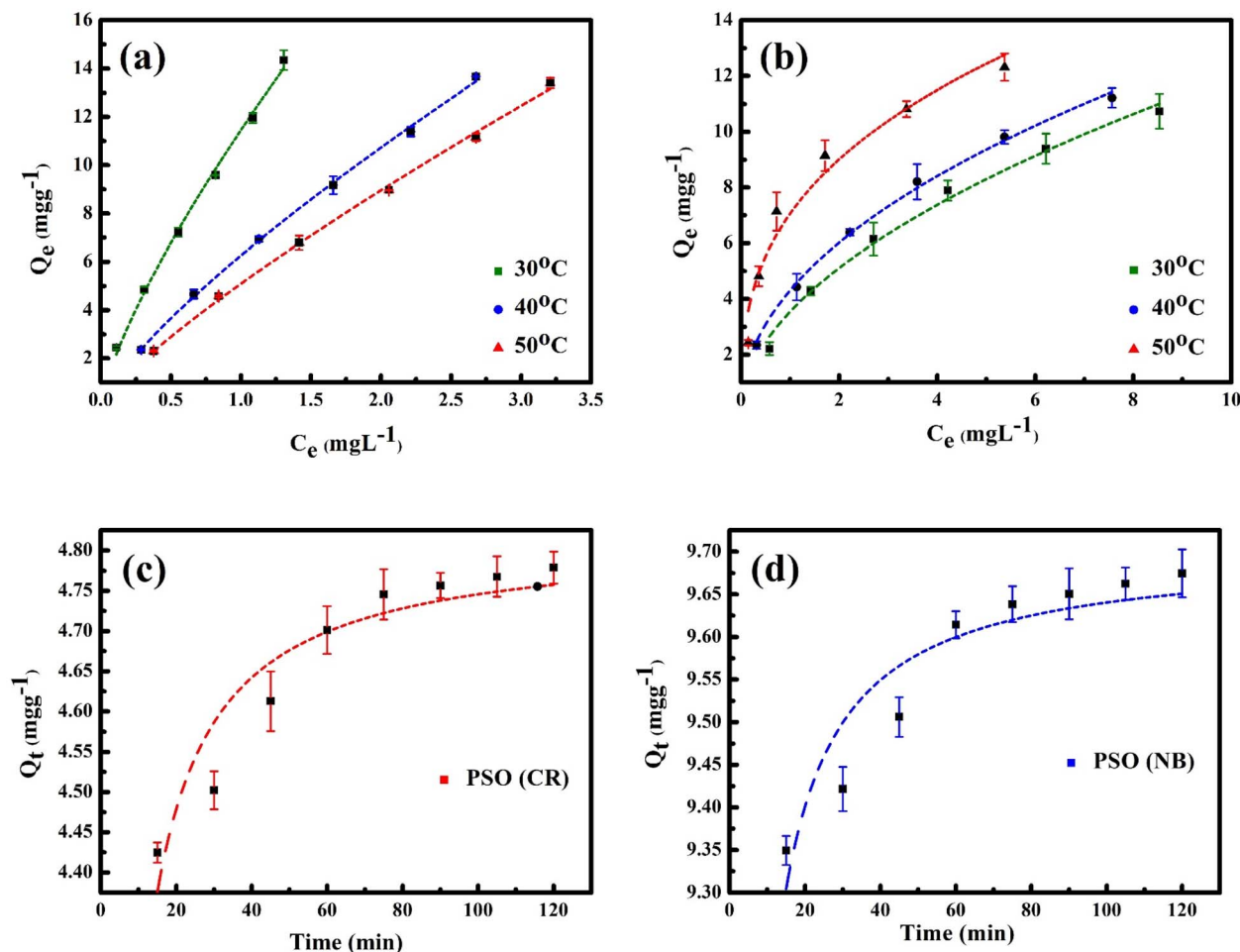


Fig. 6 Non-linear Freundlich isotherm plots for (a) CR, and (b) NB adsorption; non-linear pseudo-second order plots for (c) CR, and (d) NB adsorption.



sorption for intermediary to highly concentrated systems, and supports mechanism that follows heterogeneous Gaussian energy distribution onto specific adsorptive sites.<sup>113</sup> The activity coefficients,  $k_{D-R}$  ( $=\beta R^2 T^2$ ), for both CR and NB sorption at 30, 40, and 50 °C were interpreted, from non-linear  $Q_e$  vs.  $C_e$  D-R plots (Fig. S5e and f). A decrease in the maximum (theoretical) equilibrium monolayer sorption capacity,  $Q_{D-R}$ , (from 15.894 to 13.849 mg g<sup>-1</sup>), and free energy,  $E_{D-R}$  (from 2.248 to 1.336 kJ mol<sup>-1</sup>) with temperature was observed for CR sorption that indicated an exothermic nature, where  $E_{D-R} = (2\beta)^{-0.5}$ , and  $\beta$  (kJ<sup>-2</sup> mol<sup>2</sup>) is a constant related to adsorption energy. However, both  $Q_{D-R}$  and  $E_{D-R}$  values slightly increased in the range 9.853–11.185 mg g<sup>-1</sup> and 1.028–2.758 kJ mol<sup>-1</sup>, respectively, with a rise in temperature from 30–50 °C, indicating endothermic NB adsorption onto the GG/ $\gamma$ -Fe<sub>2</sub>O<sub>3</sub>. The D-R isotherm also gave low values of  $E_{D-R}$ , < 8 kJ mol<sup>-1</sup>, suggesting physisorption of CR and NB onto the GG/ $\gamma$ -Fe<sub>2</sub>O<sub>3</sub> at three test temperatures.

Furthermore, the comparison of  $\chi^2$ , for various non-linear isotherms, established the lowest value for the Freundlich isotherm for both CR and NB sorption, in addition to the highest  $R^2$  values for CR adsorption, and high values for NB adsorption as well. The fitting of experimental sorption data was more pronounced for the Freundlich isotherm compared to the Langmuir, Temkin, and D-R isotherms. Thereby, adsorption of both CR and NB from their aqueous solution onto GG/ $\gamma$ -Fe<sub>2</sub>O<sub>3</sub> was satisfactorily described by the Freundlich isotherm, reflecting physical nature of sorption on the energetically heterogeneous surface of GG/ $\gamma$ -Fe<sub>2</sub>O<sub>3</sub>. Appearance of heterogeneity might be a result of non-homogeneous distribution of adsorptive sites on the GG/ $\gamma$ -Fe<sub>2</sub>O<sub>3</sub> surface, which was cross-referred and found in order with the SEM (Fig. 2b), and TEM micrographs (Fig. 4).

**3.4.4. Investigation of sorption kinetics.** An insight into the kinetics of the sorption reaction was devised from the dynamic parameters that regulate the overall rate of transportation of CR/NB ions from the aqueous phase onto the surface of GG/ $\gamma$ -Fe<sub>2</sub>O<sub>3</sub>. The kinetic data, for 15–120 min duration at 30 °C for 10 mg L<sup>-1</sup> CR and 20 mg L<sup>-1</sup> NB solutions with 2.0 g L<sup>-1</sup> GG/ $\gamma$ -Fe<sub>2</sub>O<sub>3</sub>, were monitored at intervals of 15 min, and then fitted into pseudo-first order (PFO), pseudo-second order (PSO), Elovich (Table 2), intraparticle diffusion (IPD), and Boyd's liquid film diffusion (LFD) models (Table S8). The adequacy of each model was examined from  $R^2$  and  $\chi^2$  values [eqn (14) and (15)].

**3.4.4.1. Pseudo-first order kinetic model.** Lagergren and Ho's pseudo-first order kinetic model (PFO) assumes that the number of available or unoccupied adsorption sites is the sole governing parameter of the rate of reaction on the solid surface in a liquid–solid system. The parameters,  $k_1$  (min<sup>-1</sup>), PFO rate constant;  $Q_e$  and  $Q_t$  (mg g<sup>-1</sup>), the equilibrium sorption capacity, and sorption uptake at time  $t$ , respectively, were determined from the non-linear plot of  $Q_t$  and  $t$ .<sup>114</sup> The plots (Fig. S6a and b) produced comparable calculated and experimental  $Q_e$  values, but with inferior  $R^2$ . The rate constant  $k_1$  was found to be 0.183 and 0.241 min<sup>-1</sup> for CR and NB removal, respectively (Table 2).

**3.4.4.2. Pseudo-second order kinetic model.** Ho and McKay's pseudo-second order kinetic model (PSO) assumes that in addition to the adsorption surface sites, the concentration of

pollutant in the aqueous phase also determine the rate of the whole sorption process. At equilibrium, the rate-determining step (RDS) exemplifies the square of the difference between the total sorption sites and the unoccupied ones. The nature of chemical interaction between the pollutant and the surface sites controls the process.<sup>103</sup>  $Q_t$  vs.  $t$  plots (Fig. 6c and d) gave the pseudo-second order rate constant,  $k_2$  (g mg<sup>-1</sup> min<sup>-1</sup>), and equilibrium sorption capacity,  $Q_e$ .<sup>114</sup> The parameters obtained from these plots showed fair agreement between the experimental  $Q_e$  (4.701 mg g<sup>-1</sup> for CR, and 9.614 mg g<sup>-1</sup> for NB) and calculated  $Q_e$  (4.817 mg g<sup>-1</sup> for CR, and 9.702 mg g<sup>-1</sup> for NB) values, greater  $R^2$ , and lowest  $\chi^2$  values in comparison to PFO plots (Table 2). Therefore, there was a clear-cut indication in favour of site-specific chemical interactions between CR or NB and functional groups on the GG/ $\gamma$ -Fe<sub>2</sub>O<sub>3</sub> surface following PSO kinetics. This observation could be justified from the accuracy of the established resemblance between the PSO kinetic equation and the universal rate law for a chemical reaction,<sup>115</sup> alongwith the FT-IR interpretations (Fig. 1A).

**3.4.4.3. Elovich kinetic model.** The Elovich model focuses on the chemical interaction between the functional sites on the liquid–solid interface. The model assumes energetically heterogeneous adsorption without sideways interaction.<sup>116</sup> The Elovich coefficients,  $\alpha$  (mg g<sup>-1</sup> min<sup>-1</sup>) and  $\beta$  (g mg<sup>-1</sup>), exemplify the initial rate of adsorption and desorption, respectively. Moreover,  $\beta$  also signifies the extent of surface coverage and corresponding energy of activation for the chemisorption process. The non-linear  $Q_t$  vs.  $t$  plots,<sup>117</sup> for Elovich model (Fig. S6c and d), provided value of  $\alpha$  parameter ( $1.995 \times 10^8$  mg g<sup>-1</sup> min<sup>-1</sup> for CR, and  $3.867 \times 10^{21}$  mg g<sup>-1</sup> min<sup>-1</sup> for NB) much greater than  $\beta$  (5.324 g mg<sup>-1</sup> for CR, and 5.802 g mg<sup>-1</sup> for NB) (Table 2), suggesting viability and feasibility of CR and NB sorption at the GG/ $\gamma$ -Fe<sub>2</sub>O<sub>3</sub> specific sites with higher rate of adsorption than desorption.

**3.4.4.5. Adsorption mechanism.** Various factors influence the adsorption mechanism, including the nature of the solid surface, active sites, functionality, charge, and structure of the dyes, as well as interactions between the solid and pollutant interfaces.<sup>103</sup> The shifting, weakening, and appearance of distinctive peaks in the FT-IR spectra of dye-loaded GG/ $\gamma$ -Fe<sub>2</sub>O<sub>3</sub>, *i.e.*, GG/ $\gamma$ -Fe<sub>2</sub>O<sub>3</sub>@CR, and GG/ $\gamma$ -Fe<sub>2</sub>O<sub>3</sub>@NB when compared to the values for virgin GG/ $\gamma$ -Fe<sub>2</sub>O<sub>3</sub> (Fig. S7) indicated the prevalence of variable covalent/ionic/hydrogen bonding interactions, owing to involvement of O–H, C=O, *etc.* groups in bonding which influence the adsorption of CR and NB.<sup>62</sup> For instance, the peak at 3378 cm<sup>-1</sup> in the GG/ $\gamma$ -Fe<sub>2</sub>O<sub>3</sub> shifted to a lower wavenumber, 3368 cm<sup>-1</sup> in the GG/ $\gamma$ -Fe<sub>2</sub>O<sub>3</sub>@CR and 3354 cm<sup>-1</sup> in GG/ $\gamma$ -Fe<sub>2</sub>O<sub>3</sub>@NB, due to extended hydrogen bonding.<sup>27</sup> Moreover, the peak at 1622 cm<sup>-1</sup> was assigned to O–H bending vibration in GG/ $\gamma$ -Fe<sub>2</sub>O<sub>3</sub> alongside N=N stretching of azo bonds in CR.<sup>118</sup> However, no significant change in C–H stretching frequencies was discerned, and an additional peak at 1231 cm<sup>-1</sup> was ascertained for GG/ $\gamma$ -Fe<sub>2</sub>O<sub>3</sub>@CR for S=O stretch due to the –SO<sub>3</sub><sup>-</sup> group in CR.<sup>119</sup> The strong molecular bonding interactions between  $\gamma$ -Fe<sub>2</sub>O<sub>3</sub> and functional groups on GG (–OH, –CO–, –COOH), as indicated by FT-IR spectra and XPS analysis, contributed to its stability and prevented any leaching



Table 2 Kinetic parameters derived from non-linear kinetic plots for CR and NB adsorption onto GG/ $\gamma$ -Fe<sub>2</sub>O<sub>3</sub>

Pollutant	Pseudo-first order $Q_t = Q_e(1 - e^{-k_1 t})$				Pseudo-second order $Q_t = \frac{k_2 Q_e^2 t}{(1 + k_2 Q_e t)}$					Elovich $Q_t = \frac{1}{\beta} \ln(\alpha \beta t + 1)$			
	$Q_e$ (cal.) (mg g <sup>-1</sup> )	$k_1$ (min <sup>-1</sup> )	$R^2$	$\chi^2$	$Q_e$ (exp.) (mg g <sup>-1</sup> )	$Q_e$ (cal.) (mg g <sup>-1</sup> )	$k_2$ (g mg <sup>-1</sup> min <sup>-1</sup> )	$R^2$	$\chi^2$	$\alpha$ (mg g <sup>-1</sup> min <sup>-1</sup> )	$\beta$ (g mg <sup>-1</sup> )	$R^2$	$\chi^2$
CR	4.701	0.183	0.484	0.009	4.701	4.817	0.137	0.876	0.002	$1.995 \times 10^8$	5.324	0.960	$7.227 \times 10^{-4}$
NB	9.598	0.241	0.435	0.009	9.614	9.702	0.161	0.854	0.002	$3.867 \times 10^{21}$	5.802	0.952	$7.311 \times 10^{-4}$

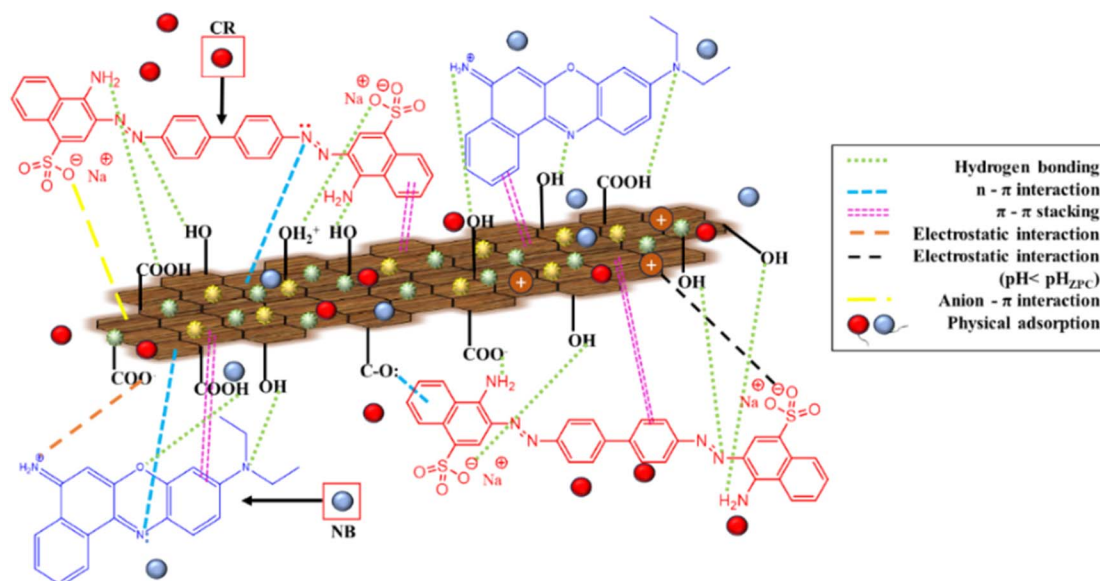
possibility of the composite in water during adsorption.<sup>62</sup> Thus, the commendable adsorption performance of GG/ $\gamma$ -Fe<sub>2</sub>O<sub>3</sub> for both CR and NB might be the consequence of FT-IR established extensive functional sites on the GG/ $\gamma$ -Fe<sub>2</sub>O<sub>3</sub> surface, and their specific interaction through several interactive pathways. Furthermore, the presence of charge on dyes, and GG/ $\gamma$ -Fe<sub>2</sub>O<sub>3</sub> surface over and above the ZPC<sup>120</sup> might have also paved the way to additional weak physical, and non-specific bonding interactions, *viz.*, van der Waals, n- $\pi$ , anion- $\pi$ , and  $\pi$ - $\pi$  stacking in addition to previously confirmed electrostatic and hydrogen bonding interactions (Fig. 7). The strength of these forces was confirmed from the bonding energy pattern obtained from the Temkin and D-R isotherms, alongside the thermodynamic investigations.

From a mechanistic viewpoint, analysis of steps governing the adsorption process becomes an indispensable task. A detailed exploration suggested that the adsorption process could be controlled by either a mass action mechanism or a chemical action (IPD/LFD). The former was realised as irrelevant considering physisorption to be a fast phenomenon.<sup>121</sup> Thus, the kinetic data was fitted to the Webber-Morris and Boyd relationships to assert whether the diffusion mechanism underlying physisorption for CR and NB removal by GG/ $\gamma$ -Fe<sub>2</sub>O<sub>3</sub>

followed (a) intraparticle diffusion (IPD), or (b) liquid film diffusion (LFD) kinetics, or (c) a simultaneous combination of both processes covering all the interior and exterior surface pores of the adsorbent by the pollutant ions.

**3.4.5.1. Intraparticle diffusion.** The Intraparticle diffusion (IPD) model is validated for those systems in which rapid adsorption takes place, such that the pollutant diffuses through the surface into the interstitial pores of the adsorbent, and binds through physical/chemical bonds, which is characterized as the RDS. This phenomenon is well understood by fitting sorption data into the Weber and Morris equation<sup>122</sup> [eqn (S4)].

The linear IPD plots, for both CR and NB, did not pass through the origin, which suggested that IPD was not the sole RDS (Fig. S8a and b).<sup>123</sup> Moreover, the plots depicted three linear regions for both dyes, the initial portion incorporated the diffusion of dyes into the exterior surface-active sites, followed by their gradual intrusion into the interstitial pores which later slowed down following unavailability of sorptive sites and diminished dye concentration, subjugating a three-step mechanism, and thus the multilinearity.<sup>124</sup> In addition, the value of intercept *C* (Table S8) for NB (9.178) was superior to that for CR (4.240), indicative of significant coverage at the boundary layer of GG/ $\gamma$ -Fe<sub>2</sub>O<sub>3</sub> on account of driving diffusion of NB.

Fig. 7 Plausible mechanism for the adsorption of CR and NB by GG/ $\gamma$ -Fe<sub>2</sub>O<sub>3</sub>.

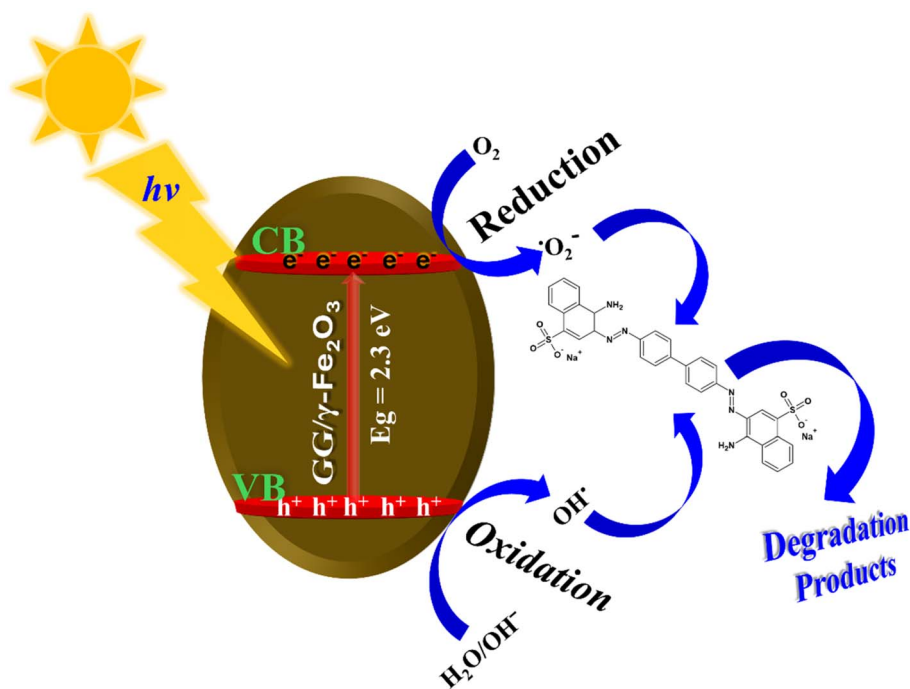


Fig. 8 Proposed mechanism for photodegradation of azo-CR by GG/γ-Fe<sub>2</sub>O<sub>3</sub>.

**3.4.5.2. Liquid film diffusion.** The Liquid film diffusion (LFD) model holds good for adsorption systems in which mass diffusion/crossing of the boundary layer by the external liquid film of pollutant from the bulk, formulated around the solid interface and the surface-active sites is established as the RDS. The phenomenon can be justified using Boyd's equation<sup>116</sup> [eqn (S5)].

The LFD plots showed linearity for CR and NB sorption but deviated from the origin, yielding a non-zero intercept value, which clarified that the adsorption was not solely governed by the film diffusion kinetics (Fig. S8c and d). The  $k_{LFD}$  and  $R^2$  values are given in Table S8.

The foregoing observations suggested a specific chemical interaction of CR and NB with functional sites on the GG/γ-Fe<sub>2</sub>O<sub>3</sub>, which was found in coincidence with those from the PSO kinetic model. Thereby, it can be concluded that both CR and NB adsorption on GG/γ-Fe<sub>2</sub>O<sub>3</sub> surface was governed partially by intraparticle as well as film diffusion steps, supplementing bulk transport and adsorptive attachment.

### 3.5. Photodegradation of CR dye, kinetics, and degradation mechanism

The photodegradation of azo-group-containing CR using GG/γ-Fe<sub>2</sub>O<sub>3</sub> catalyst was performed at 38 °C under sunlight. From the time-dependent UV-visible absorption spectra, the absorbance of the CR solutions decreased over time upon degradation (Fig. S9a). The rate of dye degradation was consistent, and nearly 50% of the CR was degraded within the first 80 min, while up to 92.7% degradation was observed during 160 min of irradiation. This high rate of degradation might be a result of a prominent band gap of the GG/γ-Fe<sub>2</sub>O<sub>3</sub>. The PFO kinetics plot (Fig. S9b) of  $\ln C_t/C_0$  vs. time  $t$  (min) produced a straight line

with rate constant  $0.014 \text{ min}^{-1}$  and  $R^2 = 0.877$ , indicating obedience to the PFO degradation mechanism. In contrast, the adsorption of CR over the GG/γ-Fe<sub>2</sub>O<sub>3</sub> surface followed PSO kinetics. Therefore, the complete removal of CR could be attributed to the simultaneous adsorption in the dark, followed by photocatalytic degradation under sunlight.

From the mechanistic notion, it can be impounded that on absorption of solar radiation of energy  $h\nu$ , more than the band gap energy, the electrons ( $e^-$ ) are excited from valence band (VB) to conduction band (CB), with simultaneous accumulation of electrons in CB, and holes ( $h^+$ ) in VB, respectively.<sup>125</sup> Fe<sup>3+</sup> ions have been reported previously to suppress the electro-hole recombination rate, because besides serving as active sites for adsorption and activation, the d-orbitals in Fe<sup>3+</sup> sites can also enhance the charge transfer efficiency.<sup>126</sup> The dissolved oxygen (O<sub>2</sub>) gets reduced by the photo-induced electrons into superoxide radical anion (O<sub>2</sub><sup>·-</sup>). Moreover, the positively charged holes oxidize H<sub>2</sub>O to OH<sup>·</sup>.<sup>127</sup> Further, to gain complete insight of the photodegradation mechanism, the catalytic effect of active species was investigated through free radical trapping experiment (Fig. S10). The CR degradation involving GG/γ-Fe<sub>2</sub>O<sub>3</sub> was considerably inhibited by scavengers in order: EDTA ( $h^+$ ) < BQ (O<sub>2</sub><sup>·-</sup>) < IPA (OH<sup>·</sup>). The results revealed that the CR percentage degradation was primarily influenced by OH<sup>·</sup> and O<sub>2</sub><sup>·-</sup> oxidative species, followed by the holes ( $h^+$ ). These highly reactive oxygen species (ROS) are powerful oxidants for complete mineralization of CR to simple degradation products, like CO<sub>2</sub>, H<sub>2</sub>O, NH<sub>4</sub><sup>+</sup>, NO<sub>3</sub><sup>-</sup>, SO<sub>4</sub><sup>2-</sup>, and mineral acids (Fig. 8). Furthermore, Fe<sub>2</sub>O<sub>3</sub> and its nanocomposites have been extensively reported as efficient photocatalysts for dye degradation.<sup>128–130</sup>

In order to determine the possible degradation intermediates, a time-based LC-MS analysis (Fig. S11) of photodegraded



diazo-CR dye solution, at optimum experimental conditions, was examined. The major intermediate species formed during CR degradation, detected by LC-MS, are shown in the Scheme 2. During the initial analysis, partial cleavage of the azo ( $-N=N-$ ) bond or modification of side groups in CR might produce large high-mass aromatic fragments. Further, breakdown of large fragments resulted in complete azo bond scission, desulphonation and deamination following  $-C-S-/C-N-$  bond cleavage, hydroxylation, azo reduction, oxidation, rearrangements, and cleavage of  $-C-C-$  bonds between the chromophore rings.<sup>5,131–135</sup> This step produced various intermediates and their derivatives, including 4-aminonaphthalene-1-sulphonic acid (ANSA,  $m/z = 246.26$ ), 4,4'-diaminobiphenyl (benzidine,  $m/z = 184.84$ ), aniline-4-sulphonic acid (sulphanilic acid,  $m/z = 172.11$ ), biphenyl ( $m/z = 150.99$ ), 1-naphthylamine/2-naphthylamine ( $m/z = 141.13$ ), aniline ( $m/z = 90.92$ ), benzene-1-ylum ( $m/z = 77.05$ ), benzene ( $m/z = 78$ ), etc. Later, the oxidative ring opening steps formed low molecular weight aromatics, acid/amine intermediates, polyphenols, and ultimately mineralized into  $CO_2$ ,  $H_2O$ ,  $NH_4^+$ ,  $NO_3^-$ , and  $SO_4^{2-}$ .

### 3.6. Real water analysis and competitive removal of CR and NB dyes

The adsorption/degradation tendency of the GG/ $\gamma$ - $Fe_2O_3$  for CR and NB amidst different water environments and co-existing ions is shown in Table S9. The removal efficiency hinders in natural wastewater samples due to the competition between large number of co-existing pollutants (organic, inorganic, and microorganisms) that compete for limited available surface-active sites. The % CR and NB removal decreased in tap water and sewage water, in comparison to RO water or distilled water, due to more competitive effect.

Typically, the solubility of organic contaminants decreases with the addition of salts (ions) owing to self-aggregation, *i.e.*, salting-out or primary kinetic salt effect.<sup>136</sup> This limits the dye solubility due to fewer available water molecules. However, the CR adsorption remained largely unaffected in the presence of salts. The results showed little effect of co-existing ions on CR adsorption (except that of  $CO_3^{2-}$ ), indicating excellent resistance of GG/ $\gamma$ - $Fe_2O_3$  to ion interference, and thus confirming specific CR adsorption by GG/ $\gamma$ - $Fe_2O_3$ . The interference by  $CO_3^{2-}$  might be mainly due its interaction with CR, and not salting.<sup>136</sup> Moreover, the inhibitory effect of divalent  $CO_3^{2-}$  (most) and  $SO_4^{2-}$  on CR adsorption/degradation were greater than monovalent  $Cl^-$  or  $NO_3^-$ , which can be attributed to strong electrostatic attractions between GG/ $\gamma$ - $Fe_2O_3$  and the higher anions, under similar conditions.<sup>137</sup> Similar observations were drawn for NB adsorption. Additionally,  $CO_3^{2-}$  ions highly and negatively affected percentage CR degradation, due to the hydrolysis of  $HCO_3^-$ , an  $OH^-$  scavenger.<sup>138</sup> Moreover, percentage NB adsorption decreased around cations *vis-à-vis* anions, suggesting higher cationic interface potential for cationic NB adsorption surfacing weak electrostatic interactions. Previous studies have shown that both CR and NB undergo stable complexation with metal ions which can affect their adsorption/degradation onto support materials in

presence of different ions.<sup>139</sup> Furthermore, the competitive influence of other anionic and cationic dyes on the CR and NB removal by GG/ $\gamma$ - $Fe_2O_3$  from a mixture is shown in Table S10. The results showed the specificity and efficiency of GG/ $\gamma$ - $Fe_2O_3$  towards CR and NB adsorption, and substantial potential in wastewater treatment.

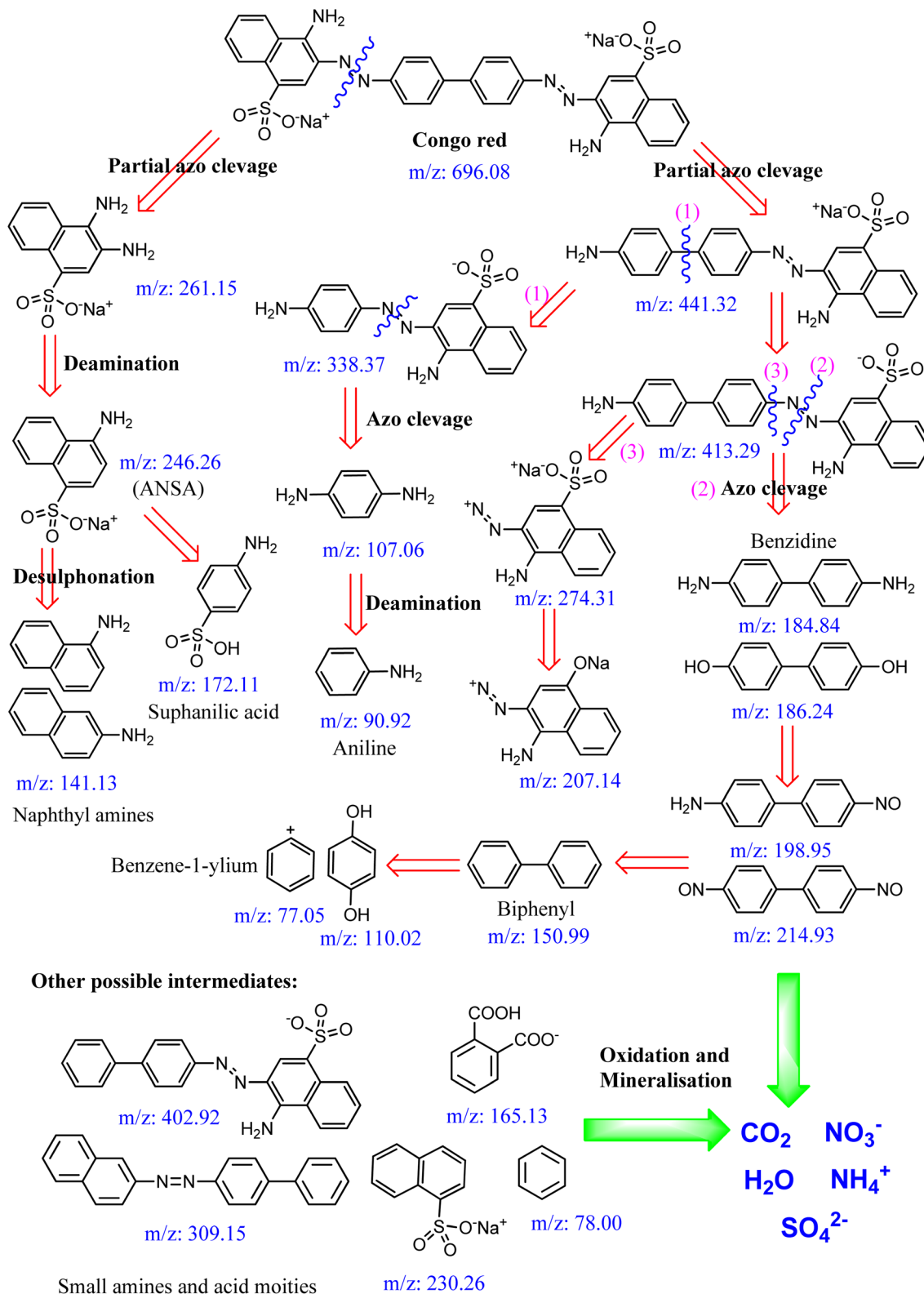
### 3.7. Regeneration and reusability of GG/ $\gamma$ - $Fe_2O_3$

Fig. S12 shows the reusability results of the GG/ $\gamma$ - $Fe_2O_3$  for CR and NB adsorption up to six cycles. The GG/ $\gamma$ - $Fe_2O_3$  was found efficient till six consecutive cycles for CR (97.12% to 76.27%), and up to 3 cycles for NB (97.12% to 71.28%). Therefore, the GG/ $\gamma$ - $Fe_2O_3$  can be more efficiently used for CR, *i.e.*, anionic dye than NB, *i.e.*, cationic dye, sorption for potential practical applications. Further, the FT-IR analysis of the spent GG/ $\gamma$ - $Fe_2O_3$  after CR adsorption (spent GG/ $\gamma$ - $Fe_2O_3$ @CR) and NB adsorption (spent GG/ $\gamma$ - $Fe_2O_3$ @NB), Fig. S7, exhibited comparable peak positions to pristine GG/ $\gamma$ - $Fe_2O_3$ , establishing appreciable structural and functional stability.

### 3.8. Cost analysis of GG/ $\gamma$ - $Fe_2O_3$

The commercial and large-scale implementation of the GG/ $\gamma$ - $Fe_2O_3$  for dye remediation from industrial effluents widely depends on its cost-effectiveness. The study addresses detailed stepwise consideration of economic feasibility through (a) the cost of synthesis of GG/ $\gamma$ - $Fe_2O_3$  per batch (on laboratory scale) (Table S11), and (b) their processing cost for use as an adsorbent/catalyst for treating 1000 L of wastewater using GG/ $\gamma$ - $Fe_2O_3$  (Table S12). The synthetic one-pot coprecipitation approach is comparatively simpler and cost-efficient in comparison to other sophisticated methods.<sup>44</sup> The *Glycyrrhiza glabra* roots were locally sourced at negligible cost, and were not subjected to any sort of energy-intensive chemical pre-treatment or post synthetic modification through expensive surfactants, toxic solvents, reagents/chemicals or synthetic stabilizers for a greener approach. Additionally, the energy consumption, limited to heating/drying, magnetic stirring, and calcination was moderate, scalable for industrial level production. The lab scale production of the GG/ $\gamma$ - $Fe_2O_3$  was estimated around \$0.79 to \$0.88, which is significantly lower than the previously reported commercial materials, including silver nanoparticles (\$15.77) and nanopowders (\$20.42) for similar applications.<sup>140,141</sup> The majority of synthesis expense was due to analytical lab-grade  $\gamma$ - $Fe_2O_3$  precursors of high purity, which can be drastically reduced by up to 100 times on large scale using industrial-grade reagents. From the perspective of treatment cost, \$158 to \$176 was estimated to treat 1000 L wastewater using optimum dosage  $0.2 \text{ g L}^{-1}$  of GG/ $\gamma$ - $Fe_2O_3$ , considering unit synthesis cost of GG/ $\gamma$ - $Fe_2O_3$  for adsorption. Solar-photocatalysis was employed for dye degradation, which cuts down the power consumption. Considering practically feasible regeneration up to four cycles, the effective treatment cost reduced by 70–80%, in range \$31.6 to \$52.8 per 1000 L of wastewater.



Scheme 2 Proposed degradation pathways of CR by GG/ $\gamma$ -Fe<sub>2</sub>O<sub>3</sub>.

### 3.9. Comparison study

The comparative evaluation of GG/ $\gamma$ -Fe<sub>2</sub>O<sub>3</sub> adsorbent/photocatalyst's efficiency in CR and NB dyes remediation was

estimated with reference to the available literature (Tables S13 and S14). The greater effectiveness of the GG/ $\gamma$ -Fe<sub>2</sub>O<sub>3</sub>, in comparison to previously studied materials, established its

wider applicability. This validation, supported by cost-effectiveness due to simple synthetic approach, and implementation of highly accessible precursors accounts for potential reliability in realistic and practical scenario.

## 4 Conclusions and future prospects

In summary, a structurally, thermally, and functionally stable GG/ $\gamma$ -Fe<sub>2</sub>O<sub>3</sub> nanocomposite was synthesized *in situ via* simple co-precipitation method, and employed for subsequent adsorption and photodegradation of CR and NB dyes, with pursuit of superior antimicrobial activity compared to the parent precursor GG. Both CR and NB dyes are extremely hazardous water pollutants that find application in various industries. The GG/ $\gamma$ -Fe<sub>2</sub>O<sub>3</sub> facilitated appreciable sorption capacity ( $Q_0$ ) of 47.504 mg g<sup>-1</sup>, and 15.361 mg g<sup>-1</sup> for CR and NB at 50 and 30 °C, respectively, achieving 99.78% and 97.23% decolorization of CR and NB, respectively, through adsorption under optimized conditions. The nanocomposite provided 92.7% degradation of CR in 160 min with a pseudo-first order rate constant of 0.014 min<sup>-1</sup>, dominated by OH<sup>•</sup> and O<sub>2</sub><sup>•-</sup> active species. The applicability of the GG/ $\gamma$ -Fe<sub>2</sub>O<sub>3</sub> for real wastewater treatment amongst competing ions and dye mixtures, under the same set of optimized experimental conditions illustrate the reliability and transferability of these conditions for large-scale application, while achieving balance between selectivity and efficiency. The comparative economic and evaluative performance of the GG/ $\gamma$ -Fe<sub>2</sub>O<sub>3</sub> with previously synthesized materials, accompanied by regenerative tendency and FT-IR affirmed stability of spent GG/ $\gamma$ -Fe<sub>2</sub>O<sub>3</sub> post treatment indicated significant potential in water treatment. Overall, the study bridges laboratory outcomes with practical applications and contributes to the development of advanced multifunctional materials for decolourising dye-laden industrial wastewater.

However, a proper post-treatment disposal strategy, for the composite, should be designed considering environmental sustainability. Additionally, changes in total organic carbon (TOC) and water quality parameters should be investigated to determine the mineralization efficiency after dye degradation. The future work may address the integration of GG/ $\gamma$ -Fe<sub>2</sub>O<sub>3</sub> for continuous flow or field-scale treatment systems.

## Author contributions

Ankita Manchanda: conceptualization, visualisation, formal analysis, investigation, methodology, software, data curation, writing-original draft, funding acquisition. Ahmed Hussain Jawhari: data curation, validation. Ziaul Hasan: conceptualization, investigation. Nazim Hasan: data curation, validation. Sneha Shukla: validation. Adiba Khan: validation. Tabrez Alam Khan: supervision, writing-review & editing. Saif Ali Chaudhry: supervision, project administration, resources, writing-review & editing.

## Conflicts of interest

There are no conflicts of interest to declare.

## Data availability

The authors confirm that the data supporting the findings of the study are available within the article and in its supplementary information (SI). Supplementary information is available. See DOI: <https://doi.org/10.1039/d5ra04982b>.

## Acknowledgements

The authors highly acknowledge Jamia Millia Islamia, New Delhi, for providing laboratory facilities. Ankita Manchanda expresses her gratitude to the Department of Science and Technology (DST), New Delhi, India, for financial support through INSPIRE fellowship (IF200064), and Saif Ali Chaudhry acknowledges financial support by DST-SERB (EEQ/2022/001063).

## References

- 1 D. Dutta, S. Arya and S. Kumar, Industrial wastewater treatment: current trends, bottlenecks, and best practices, *Chemosphere*, 2021, **285**, 131245.
- 2 W. A. Shaikh, R. U. Islam and S. Chakraborty, Stable silver nanoparticle doped mesoporous biochar-based nanocomposite for efficient removal of toxic dyes, *J. Environ. Chem. Eng.*, 2021, **9**, 104982.
- 3 *Top Dyes and Pigments Companies in Global [Updated]* Global Growth Insights, <https://www.globalgrowthinsights.com/blog/dyes-and-pigments-companies-733>, accessed 18 June 2025.
- 4 S. Moosavi, C. W. Lai, S. Gan, G. Zamiri, O. A. Pivzhani and M. R. Johan, Application of efficient magnetic particles and activated carbon for dye removal from wastewater, *ACS Omega*, 2020, **5**, 20684–20697.
- 5 P. Yadav, N. Dhariwal, M. Kumari, V. Kumar and O. P. Thakur, Enhanced degradation of Congo-red dye by Cr<sup>3+</sup> doped  $\alpha$ -Fe<sub>2</sub>O<sub>3</sub> nano-particles under sunlight and industrial wastewater treatment, *Chemosphere*, 2023, **343**, 140208.
- 6 S. Meneceur, H. Hemmami, A. Bouafia, S. E. Laouini, M. L. Tedjani, D. Berra and M. S. Mahboub, Photocatalytic activity of iron oxide nanoparticles synthesized by different plant extracts for the degradation of diazo dyes Evans blue and Congo red, *Biomass Convers. Biorefin.*, 2024, **14**, 5357–5372.
- 7 G. Sarojini, S. V. Babu and M. Rajasimman, Adsorptive potential of iron oxide-based nanocomposite for the sequestration of Congo red from aqueous solution, *Chemosphere*, 2022, **287**, 132371.
- 8 N. Natasha, A. Khan, U. U. Rahman, N. Sadaf, M. Yaseen, R. A. Abumousa, R. Khattak, N. Rehman, M. Bououdina and M. Humayun, Effective Removal of Nile Blue Dye from Wastewater using Silver-Decorated Reduced Graphene Oxide, *ACS Omega*, 2024, **9**, 19461–19480.
- 9 E. Jafarian, A. Hekmatian, A. Cheraghdar, H. Safarzadeh and M. Shamsi, Elimination performance of Nile blue from wastewater using by carboxymethyl cellulose-graft-



- poly(methacrylic acid-co-acrylamide)/kaolin nanocomposite hydrogel, *Int. J. Environ. Sci. Technol.*, 2023, **20**, 9933–9944.
- 10 A. K. Nayak and A. Pal, Statistical modeling and performance evaluation of biosorptive removal of Nile blue A by lignocellulosic agricultural waste under the application of high-strength dye concentrations, *J. Environ. Chem. Eng.*, 2020, **8**, 103677.
  - 11 D. Hussain, S. A. Khan, T. A. Khan and S. S. Alharthi, Efficient liquid phase confiscation of nile blue using a novel hybrid nanocomposite synthesized from guar gum-polyacrylamide and erbium oxide, *Sci. Rep.*, 2022, **12**, 14656.
  - 12 A. Iqbal, A. Yusaf, M. Usman, T. H. Bokhari and A. Mansha, Insight into the degradation of different classes of dyes by advanced oxidation processes; a detailed review, *Int. J. Environ. Anal. Chem.*, 2023, 5503–5537.
  - 13 R. Gusain, K. Gupta, P. Joshi and O. P. Khatri, Adsorptive removal and photocatalytic degradation of organic pollutants using metal oxides and their composites: a comprehensive review, *Adv. Colloid Interface Sci.*, 2019, **272**, 102009.
  - 14 B. Lellis, C. Z. Fávaro-Polonio, J. A. Pamphile and J. C. Polonio, Effects of textile dyes on health and the environment and bioremediation potential of living organisms, *Biotechnol. Res. Innov.*, 2019, **3**, 275–290.
  - 15 M. A. Alkhadra, X. Su, M. E. Suss, H. Tian, E. N. Guyes, A. N. Shocron, K. M. Conforti, J. P. De Souza, N. Kim, M. Tedesco, K. Khoiruddin, I. G. Wenten, J. G. Santiago, T. A. Hatton and M. Z. Bazant, Electrochemical Methods for Water Purification, Ion Separations, and Energy Conversion, *Chem. Rev.*, 2022, **122**, 13547–13635.
  - 16 P. Ganguly, R. Sarkhel and P. Das, Synthesis of pyrolyzed biochar and its application for dye removal: batch, kinetic and isotherm with linear and non-linear mathematical analysis, *Surf. Interfaces*, 2020, **20**, 100616.
  - 17 M. Wen, G. Li, H. Liu, J. Chen, T. An and H. Yamashita, Metal-organic framework-based nanomaterials for adsorption and photocatalytic degradation of gaseous pollutants: recent progress and challenges, *Environ. Sci. Nano*, 2019, **6**, 1006–1025.
  - 18 S. Nangia, D. Katyal and S. G. Warkar, Thermodynamics, kinetics and isotherm studies on the removal of anionic azo-dye (Congo red) using synthesized chitosan/Moringa oleifera gum hydrogel composites, *Sep. Sci. Technol.*, 2023, **58**, 13–28.
  - 19 S. A. Khan, A. Manchanda and T. A. Khan, Adsorption of Coomassie Brilliant Blue on a Novel Eco-Friendly Nanogel from Simulated Water: Equilibrium, Kinetic, and Thermodynamic Studies, *ChemistrySelect*, 2024, **9**, e202304927.
  - 20 M. Yaseen, M. Humayun, A. Khan, M. Idrees, N. Shah and S. Bibi, Photo-Assisted Removal of Rhodamine B and Nile Blue Dyes from Water Using CuO–SiO<sub>2</sub> Composite, *Molecules*, 2022, **27**(16), 5343.
  - 21 Y. Pi, C. Duan, Y. Zhou, S. Sun, Z. Yin, H. Zhang, C. Liu and Y. Zhao, The effective removal of Congo Red using a bio-nanocluster: Fe<sub>3</sub>O<sub>4</sub> nanoclusters modified bacteria, *J. Hazard. Mater.*, 2022, **424**, 127577.
  - 22 S. I. Siddiqui and S. A. Chaudhry, Nanohybrid composite Fe<sub>2</sub>O<sub>3</sub>-ZrO<sub>2</sub>/BC for inhibiting the growth of bacteria and adsorptive removal of arsenic and dyes from water, *J. Clean. Prod.*, 2019, **223**, 849–868.
  - 23 M. Kasbaji, I. Ibrahim, M. Mennani, O. a. abuelalla, S. S. fekry, M. M. Mohamed, T. M. Salama, I. A. Moneam, M. Mbarkhi, A. Moubarik and M. Oubenali, Future trends in dye removal by metal oxides and their nano/composites: a comprehensive review, *Inorg. Chem. Commun.*, 2023, **158**, 111546.
  - 24 A. Tchinsa, M. F. Hossain, T. Wang and Y. Zhou, Removal of organic pollutants from aqueous solution using metal organic frameworks (MOFs)-based adsorbents: a review, *Chemosphere*, 2021, **284**, 131393.
  - 25 K. Manzoor, M. Batool, F. Naz, M. F. Nazar, B. H. Hameed and M. N. Zafar, A comprehensive review on application of plant-based bioadsorbents for Congo red removal, *Biomass Convers. Biorefin.*, 2024, **14**, 4511–4537.
  - 26 N. Kumar, A. Pandey, Rosy and Y. C. Sharma, A review on sustainable mesoporous activated carbon as adsorbent for efficient removal of hazardous dyes from industrial wastewater, *J. Water Process Eng.*, 2023, **54**, 104054.
  - 27 L. Cheng, Y. Ji, X. Liu, L. Mu and J. Zhu, Sorption mechanism of organic dyes on a novel self-nitrogen-doped porous graphite biochar: coupling DFT calculations with experiments, *Chem. Eng. Sci.*, 2021, **242**, 116739.
  - 28 K. K. Kefeni and B. B. Mamba, Photocatalytic application of spinel ferrite nanoparticles and nanocomposites in wastewater treatment: review, *Sustain. Mater. Technol.*, 2020, **23**, e00140.
  - 29 G. Fadillah, S. P. Yudha, S. Sagadevan, I. Fatimah and O. Muraza, Magnetic iron oxide/clay nanocomposites for adsorption and catalytic oxidation in water treatment applications, *Open Chem.*, 2020, **18**, 1148–1166.
  - 30 J. Wang, Y. Chen, G. Liu and Y. Cao, Synthesis, characterization and photocatalytic activity of inexpensive and non-toxic Fe<sub>2</sub>O<sub>3</sub>–Fe<sub>3</sub>O<sub>4</sub> nano-composites supported by montmorillonite and modified by graphene, *Composites, Part B*, 2017, **114**, 211–222.
  - 31 X. Wang, L. Tang, T. Yang, Y. Shi, F. Liu and H. Jiang, Remediation of bensulfuron methyl polluted water and soil by Fe<sub>2</sub>O<sub>3</sub>/Fe<sub>3</sub>O<sub>4</sub>@C activating peroxymonosulfate: chloride enhancement effect and phytotoxicity assessment, *Chem. Eng. J.*, 2023, **474**, 145439.
  - 32 S. Yadav, K. Shakya, A. Gupta, D. Singh, A. R. Chandran, A. V. Aanappalli, K. Goyal, N. Rani and K. Saini, A review on degradation of organic dyes by using metal oxide semiconductors, *Environ. Sci. Pollut. Res.*, 2023, **30**, 71912–71932.
  - 33 S. Arsalani, E. J. Guidelli, J. F. D. F. Araujo, A. C. Bruno and O. Baffa, Green Synthesis and Surface Modification of Iron Oxide Nanoparticles with Enhanced Magnetization Using Natural Rubber Latex, *ACS Sustain. Chem. Eng.*, 2018, **6**, 13756–13765.



- 34 S. Mishra, L. Cheng and A. Maiti, The utilization of agrobio-mass/byproducts for effective bio-removal of dyes from dyeing wastewater: a comprehensive review, *J. Environ. Chem. Eng.*, 2021, **9**, 104901.
- 35 N. J. Ashbolt, Microbial Contamination of Drinking Water and Human Health from Community Water Systems, *Curr. Environ. Health Rep.*, 2015, **2**, 95–106.
- 36 N. A. Salahuddin, H. A. EL-Daly, R. G. El Sharkawy and B. T. Nasr, Nano-hybrid based on polypyrrole/chitosan/graphene oxide magnetite decoration for dual function in water remediation and its application to form fashionable colored product, *Adv. Powder Technol.*, 2020, **31**, 1587–1596.
- 37 K. Naseem, M. H. Tahir, F. Farooqi, S. Manzoor and S. U. Khan, Strategies adopted for the preparation of sodium alginate-based nanocomposites and their role as catalytic, antibacterial, and antifungal agents, *Rev. Chem. Eng.*, 2023, **39**, 1359–1391.
- 38 U. Baig, M. Faizan and M. Sajid, Effective removal of hazardous pollutants from water and deactivation of water-borne pathogens using multifunctional synthetic adsorbent materials: a review, *J. Clean. Prod.*, 2021, **302**, 126735.
- 39 T. K. Lim, *Glycyrrhiza glabra*, *Edible Medicinal and Non-medicinal Plants*, 2016, pp. 354–457.
- 40 E. Alibakhshi, M. Ramezanzadeh, S. A. Haddadi, G. Bahlakeh, B. Ramezanzadeh and M. Mahdavian, Persian liquorice extract as a highly efficient sustainable corrosion inhibitor for mild steel in sodium chloride solution, *J. Clean. Prod.*, 2019, **210**, 660–672.
- 41 A. Khan, Z. Sheerazi, S. Shukla, A. Manchanda and S. A. Chaudhry, Multifunctional nanocomposite for sustainable Yamuna water treatment: insight into adsorption, statistical optimization, and antibacterial action, *Chemosphere*, 2025, **385**, 144565.
- 42 M. Rui, C. Ma, Y. Hao, J. Guo, Y. Rui, X. Tang, Q. Zhao, X. Fan, Z. Zhang, T. Hou and S. Zhu, Iron oxide nanoparticles as a potential iron fertilizer for peanut (*Arachis hypogaea*), *Front. Plant Sci.*, 2016, **7**, 195361.
- 43 A. Saurabh, M. Kaur, R. Khan, G. Guleria, M. Shandilya and S. Thakur, Foliar application of Fe<sub>2</sub>O<sub>3</sub> nanofertilizer on growth and yield of cauliflower (*Brassica oleracea* var. Botrytis L.) cv. Pusa Snowball K-1, *Int. J. Phytoremediation*, 2024, **26**, 993–1002.
- 44 A. Herawati, R. M. Aryani, G. Antarnusa, Khoiriah and A. Nene, Fe<sub>3</sub>O<sub>4</sub>/chitosan nanocomposites for Congo red removal: adsorption surpasses photodegradation, *Mater. Chem. Phys.*, 2026, **347**, 131431.
- 45 T. Shahriari, H. Kangazian and B. A. Goharrizi, Application of Licorice-derived Activated Carbon in Tannery Wastewater Treatment, *J. Med. Plants By-Prod.*, 2024, **13**, 741–746.
- 46 S. Z. Mohammadi, H. Hamidian and Z. Moeinadini, High surface area-activated carbon from *Glycyrrhiza glabra* residue by ZnCl<sub>2</sub> activation for removal of Pb(II) and Ni(II) from water samples, *J. Ind. Eng. Chem.*, 2014, **20**, 4112–4118.
- 47 B. Ovez, S. Ozgen and M. Yuksel, Biological denitrification in drinking water using *Glycyrrhiza glabra* and *Arunda donax* as the carbon source, *Process Biochem.*, 2006, **41**, 1539–1544.
- 48 S. Pirsalami, S. Bagherpour, M. E. Bahrololoom and M. Riazi, Adsorption efficiency of *glycyrrhiza glabra* root toward heavy metal ions: experimental and molecular dynamics simulation study on removing copper ions from wastewater, *Sep. Purif. Technol.*, 2021, **275**, 119215.
- 49 A. Ramos, E. Monteiro and A. Rouboa, Biomass pre-treatment techniques for the production of biofuels using thermal conversion methods – a review, *Energy Convers. Manag.*, 2022, **270**, 116271.
- 50 A. Choudhry, A. Sharma, T. A. Khan and S. A. Chaudhry, Flax seeds based magnetic hybrid nanocomposite: an advance and sustainable material for water cleansing, *J. Water Process Eng.*, 2021, **42**, 102150.
- 51 M. Mahmoodi, B. Aslibeiki, S. Ghosh, L. Hasani, S. Slimani, L. Vattuone, D. Peddis and T. Sarkar, Apple Tree Root-Derived Biochar/Iron Oxide Triphasic Nanocomposite for Wastewater Treatment and Microwave Absorption, *Adv. Sustainable Syst.*, 2024, **9**, 2400549.
- 52 G. Sposito, On Points of Zero Charge, *Environ. Sci. Technol.*, 1998, **32**, 2815–2819.
- 53 A. Choudhry, A. Sharma, S. I. Siddiqui, I. Ahamad, M. Sajid, T. A. Khan and S. A. Chaudhry, *Origanum vulgare* manganese ferrite nanocomposite: an advanced multifunctional hybrid material for dye remediation, *Environ. Res.*, 2023, **220**, 115193.
- 54 J. H. Jorgensen and M. J. Ferraro, Antimicrobial susceptibility testing: a review of general principles and contemporary practices, *Clin. Infect. Dis.*, 2009, **49**, 1749–1755.
- 55 M. Irani, M. Sarmadi, F. Bernard, H. Ebrahimi and H. S. Bazarnov, Leaves Antimicrobial Activity of *Glycyrrhiza glabra* L, *Iran. J. Pharm. Res.*, 2010, **9**(4), 425–82010.
- 56 Z. Hasan, A. Islam and L. A. Khan, Signature Garlic Phytochemical as a Potential Anti-Candidal Candidate Targeting Virulence Factors in *Candida albicans*, *Med. Sci. Forum.*, 2023, **21**(1), 50.
- 57 W. PA, *Reference Method for Broth Dilution Antifungal Susceptibility Testing of Yeasts, Approved Standard-second edition, CLSI document M27-A2*, 2002.
- 58 M. D. Olawale, E. O. Akintemi, B. E. Agbaffa and J. A. Obaleye, Synthesis, characterization, adsorption study, quantum mechanics, monte carlo and molecular dynamics of lead based polymeric compound towards mopping of aqueous methyl red dye, *Results Chem.*, 2022, **4**, 100499.
- 59 T. A. Khan, M. Nazir and E. A. Khan, Magnetically modified multiwalled carbon nanotubes for the adsorption of bismarck brown R and Cd(II) from aqueous solution: batch and column studies, *Desalination Water Treat.*, 2016, **57**, 19374–19390.
- 60 I. Ahmad, K. Manzoor, G. Aalam, M. Amir, S. W. Ali and S. Ikram, Facile Synthesis of L-Tryptophan Functionalized Magnetic Nanophotocatalyst Supported by Copper Nanoparticles for Selective Reduction of Organic



- Pollutants and Degradation of Azo Dyes, *Catal. Lett.*, 2023, **153**, 2604–2623.
- 61 J. T. Schneider, D. S. Firak, R. R. Ribeiro and P. Peralta-Zamora, Use of scavenger agents in heterogeneous photocatalysis: truths, half-truths, and misinterpretations, *Phys. Chem. Chem. Phys.*, 2020, **22**, 15723–15733.
- 62 H. Wang, Q. Yao, C. Wang, B. Fan, Q. Sun, C. Jin, Y. Xiong and Y. Chen, A simple, one-step hydrothermal approach to durable and robust superparamagnetic, superhydrophobic and electromagnetic wave-absorbing wood, *Sci. Rep.*, 2016, **6**, 1–10.
- 63 A. Rifianto, J. Widakdo, N. Istikhomah, E. Suharyadi, T. Kato and S. Iwata, The effect of synthesis parameter on crystal structure and magnetic properties of  $\text{Ni}_{0.5}\text{Zn}_{0.5}\text{Fe}_2\text{O}_4$  magnetic nanoparticles, *J. Phys. Conf.*, 2018, **1011**, 012059.
- 64 L. Rahman, S. Bhattacharjee, S. Islam, F. Zahan, B. Biswas and N. Sharmin, A study on the preparation and characterization of maghemite ( $\gamma\text{-Fe}_2\text{O}_3$ ) particles from iron-containing waste materials, *J. Asian Ceram. Soc.*, 2020, **8**, 1083–1094.
- 65 M. M. Ba-Abbad, A. Benamour, D. Ewis, A. W. Mohammad and E. Mahmoudi, Synthesis of  $\text{Fe}_3\text{O}_4$  Nanoparticles with Different Shapes Through a Co-Precipitation Method and Their Application, *J. Met.*, 2022, **74**, 3531–3539.
- 66 F. Yang, T. Chu, Y. Zhang, X. Liu, G. Sun and Z. Chen, Quality assessment of licorice (*Glycyrrhiza glabra* L.) from different sources by multiple fingerprint profiles combined with quantitative analysis, antioxidant activity and chemometric methods, *Food Chem.*, 2020, **324**, 126854.
- 67 M. Bavanilatha, L. Yoshihita, S. Nivedhitha and S. Sahithya, Bioactive studies of  $\text{TiO}_2$  nanoparticles synthesized using *Glycyrrhiza glabra*, *Biocatal. Agric. Biotechnol.*, 2019, **19**, 101131.
- 68 A. Yousefi, S. A. S. Ebrahimi, A. Seyfoori and H. M. Hosseini, Maghemite Nanorods and Nanospheres: Synthesis and Comparative Physical and Biological Properties, *Bionanoscience*, 2018, **8**, 95–104.
- 69 Y. Huo, P. Singh, Y. J. Kim, V. Soshnikova, J. Kang, J. Markus, S. Ahn, V. Castro-Aceituno, R. Mathiyalagan, M. Chokkalingam, K. S. Bae and D. C. Yang, Biological synthesis of gold and silver chloride nanoparticles by *Glycyrrhiza uralensis* and in vitro applications, *Artif. Cells, Nanomed., Biotechnol.*, 2018, **46**, 303–312.
- 70 P. Pascuta, G. Borodi, M. Bosca, L. Pop, S. Rada and E. Culea, Preparation and structural characterization of some  $\text{Fe}_2\text{O}_3\text{-B}_2\text{O}_3\text{-ZnO}$  glasses and glass ceramics, *J. Phys.:Conf. Ser.*, 2009, **182**, 012072.
- 71 D. Liu, Z. Ma, Z. Wang, H. Tian and M. Gu, Biodegradable poly(vinyl alcohol) foams supported by cellulose nanofibrils: processing, structure, and properties, *Langmuir*, 2014, **30**, 9544–9550.
- 72 M. E. Mejia-Santillan, N. Pariona, J. Bravo-C., M. Herrera-Trejo, F. Montejo-Alvaro, A. Zarate, D. L. Perry and A. I. Mtz-Enriquez, Physical and arsenic adsorption properties of maghemite and magnetite sub-microparticles, *J. Magn. Magn. Mater.*, 2018, **451**, 594–601.
- 73 M. Arakha, S. Pal, D. Samantarrai, T. K. Panigrahi, B. C. Mallick, K. Pramanik, B. Mallick and S. Jha, Antimicrobial activity of iron oxide nanoparticle upon modulation of nanoparticle-bacteria interface, *Sci. Rep.*, 2015, **5**, 1–12.
- 74 M. Khatamian, N. A. No, S. H. Nami and S. Fazli-Shokouhi, Synthesis and characterization of zeolite A,  $\text{Fe}_3\text{O}_4$ /zeolite A, and  $\text{Fe}_2\text{O}_3$ /zeolite A nanocomposites and investigation of their arsenic removal performance, *J. Iran. Chem. Soc.*, 2023, **20**, 1657–1670.
- 75 M. Thommes, K. Kaneko, A. V. Neimark, J. P. Olivier, F. Rodriguez-Reinoso, J. Rouquerol and K. S. W. Sing, Physisorption of gases, with special reference to the evaluation of surface area and pore size distribution (IUPAC Technical Report), *Pure Appl. Chem.*, 2015, **87**, 1051–1069.
- 76 N. Srivastava, M. Srivastava, A. Alhazmi, A. Mohammad, S. Khan, D. B. Pal, S. Haque, R. Singh, P. K. Mishra and V. K. Gupta, Sustainable green approach to synthesize  $\text{Fe}_3\text{O}_4/\alpha\text{-Fe}_2\text{O}_3$  nanocomposite using waste pulp of *Syzygium cumini* and its application in functional stability of microbial cellulases, *Sci. Rep.*, 2021, **11**, 1–12.
- 77 M. Roslova, Z. Huang and X. Zou, Structural studies of inorganic materials by electron crystallography, *Comprehensive Inorganic Chemistry III*, 3rd edn, 2023, vol. 1–10, pp. 51–85.
- 78 Z. K. Heiba, S. I. Ahmed and M. B. Mohamed, Improved nonlinear optical and magnetic properties of Eu-doped nano-maghemite, *Appl. Phys. A: Mater. Sci. Process.*, 2022, **128**, 1–11.
- 79 R. Mahajan, S. Suriyanarayanan and I. A. Nicholls, Improved solvothermal synthesis of  $\gamma\text{-Fe}_2\text{O}_3$  magnetic nanoparticles for  $\text{SiO}_2$  coating, *Nanomaterials*, 2021, **11**, 1889.
- 80 Y. Li, C. Zhu, T. Lu, Z. Guo, D. Zhang, J. Ma and S. Zhu, Simple fabrication of a  $\text{Fe}_2\text{O}_3$ /carbon composite for use in a high-performance lithium ion battery, *Carbon*, 2013, **52**, 565–573.
- 81 J. P. Jyothibas, R. H. Wang, K. Ong, J. H. L. Ong and R. H. Lee, Scalable synthesis of  $\gamma\text{-Fe}_2\text{O}_3$ -based composite films as freestanding negative electrodes with ultra-high areal capacitances for high-performance asymmetric supercapacitors, *Cellulose*, 2022, **29**, 321–340.
- 82 S. Sun, M. Sun, Y. Kong, Y. Fang and Y. Yao,  $\text{MoS}_2$  and graphene as dual, cocatalysts for enhanced visible light photocatalytic activity of  $\text{Fe}_2\text{O}_3$ , *J. Sol. Gel Sci. Technol.*, 2016, **80**, 719–727.
- 83 Y. F. Huang, W. H. Kuan, P. T. Chiueh and S. L. Lo, Pyrolysis of biomass by thermal analysis–mass spectrometry (TA–MS), *Bioresour. Technol.*, 2011, **102**, 3527–3534.
- 84 F. Batool, S. Kanwal, H. Kanwal, S. Noreen, M. S. Hodhod, M. Mustaqeem, G. Sharif, H. K. Naem, J. Zahid and A. R. Z. Gaafar, Ecofriendly Synthesis of Magnetic Composites Loaded on Rice Husks for Acid Blue 25 Decontamination: Adsorption Kinetics, Thermodynamics, and Isotherms, *Molecules*, 2023, **28**, 7124.



- 85 S. Ashrafi-Saiedlou, M. H. Rasouli-Sadaghiani, M. Fattahi and Y. Ghosta, Biosynthesis and characterization of iron oxide nanoparticles fabricated using cell-free supernatant of *Pseudomonas fluorescens* for antibacterial, antifungal, antioxidant, and photocatalytic applications, *Sci. Rep.*, 2025, **15**, 1–22.
- 86 M. Shaban, M. Binsabt, A. M. Ahmed and F. Mohamed, Recycling rusty iron with natural zeolite heulandite to create a unique nanocatalyst for green hydrogen production, *Nanomaterials*, 2021, **11**, 3445.
- 87 S. Saleem, M. N. Ashiq, S. Manzoor, U. Ali, R. Liaqat, A. Algahtani, S. Mujtaba, V. Tirth, A. M. Alsuhaibani, M. S. Refat, A. Ali, M. Aslam and A. Zaman, Analysis and characterization of opto-electronic properties of iron oxide (Fe<sub>2</sub>O<sub>3</sub>) with transition metals (Co, Ni) for the use in the photodetector application, *J. Mater. Res. Technol.*, 2023, **25**, 6150–6166.
- 88 P. Kumar, U. Kumar, Y. C. Huang, P. Y. Tsai, C. H. Liu, C. H. Wu, W. M. Huang and K. L. Chen, Photocatalytic activity of a hydrothermally synthesized  $\gamma$ -Fe<sub>2</sub>O<sub>3</sub>@Au/MoS<sub>2</sub> heterostructure for organic dye degradation under green light, *J. Photochem. Photobiol., A*, 2022, **433**, 114186.
- 89 N. Zahmouli, M. Hjiri, L. El Mir, A. Bonavita, N. Donato, G. Neri and S. G. Leonardi, High performance acetone sensor based on  $\gamma$ -Fe<sub>2</sub>O<sub>3</sub>/Al-ZnO nanocomposites, *Nanotechnology*, 2018, **30**, 055502.
- 90 V. K. Gupta, A. Fatima, U. Faridi, A. S. Negi, K. Shanker, J. K. Kumar, N. Rahuja, S. Luqman, B. S. Sisodia, D. Saikia, M. P. Darokar and S. P. S. Khanuja, Antimicrobial potential of *Glycyrrhiza glabra* roots, *J. Ethnopharmacol.*, 2008, **116**, 377–380.
- 91 S. Rodino, A. Butu, M. Butu, P. Cornea and B. Marasti, Comparative studies on antibacterial activity of licorice, elderberry and dandelion, *Dig. J. Nanomater. Biostruct.*, 2015, **10**(3), 947–955.
- 92 N. T. T. Nguyen, L. M. Nguyen, T. T. T. Nguyen, T. T. Nguyen, D. T. C. Nguyen and T. Van Tran, Formation, antimicrobial activity, and biomedical performance of plant-based nanoparticles: a review, *Environ. Chem. Lett.*, 2022, **20**, 2531–2571.
- 93 G. Sharma, M. Naushad, A. Kumar, S. Rana, S. Sharma, A. Bhatnagar, F. J. Stadler, A. A. Ghfar and M. R. Khan, Efficient removal of coomassie brilliant blue R-250 dye using starch/poly(alginate-chitosan) nanohydrogel, *Process Saf. Environ. Prot.*, 2017, **109**, 301–310.
- 94 R. Nodehi, H. Shayesteh and A. R. Kelishami, Enhanced adsorption of Congo red using cationic surfactant functionalized zeolite particles, *Microchem. J.*, 2020, **153**, 104281.
- 95 C. Su, Environmental implications and applications of engineered nanoscale magnetite and its hybrid nanocomposites: a review of recent literature, *J. Hazard. Mater.*, 2017, **322**, 48–84.
- 96 J. Iqbal, N. S. Shah, M. Sayed, N. K. Niazi, M. Imran, J. A. Khan, Z. U. H. Khan, A. G. S. Hussien, K. Polychronopoulou and F. Howari, Nano-zerovalent manganese/biochar composite for the adsorptive and oxidative removal of Congo-red dye from aqueous solutions, *J. Hazard. Mater.*, 2021, **403**, 123854.
- 97 E. Rápó and S. Tonk, Factors Affecting Synthetic Dye Adsorption; Desorption Studies: A Review of Results from the Last Five Years (2017–2021), *Molecules*, 2021, **26**, 5419.
- 98 X. C. Tang, M. J. Pikal and L. S. Taylor, The Effect of Temperature on Hydrogen Bonding in Crystalline and Amorphous Phases in Dihydropyrene Calcium Channel Blockers, *Pharm. Res.*, 2002, **19**, 484–490.
- 99 M. C. S. Reddy, L. Sivaramakrishna and A. V. Reddy, The use of an agricultural waste material, Jujuba seeds for the removal of anionic dye (Congo red) from aqueous medium, *J. Hazard. Mater.*, 2012, **203–204**, 118–127.
- 100 A. Haleem, A. Shafiq, S. Q. Chen and M. Nazar, A Comprehensive Review on Adsorption, Photocatalytic and Chemical Degradation of Dyes and Nitro-Compounds over Different Kinds of Porous and Composite Materials, *Molecules*, 2023, **28**(3), 1081.
- 101 J. Nasiri, E. Motamedi, M. R. Naghavi and M. Ghafoori, Removal of crystal violet from water using  $\beta$ -cyclodextrin functionalized biogenic zero-valent iron nanoadsorbents synthesized via aqueous root extracts of *Ferula persica*, *J. Hazard. Mater.*, 2019, **367**, 325–338.
- 102 S. A. Khan, M. F. Siddiqui and T. A. Khan, Ultrasonic-assisted synthesis of polyacrylamide/bentonite hydrogel nanocomposite for the sequestration of lead and cadmium from aqueous phase: equilibrium, kinetics and thermodynamic studies, *Ultrason. Sonochem.*, 2020, **60**, 104761.
- 103 S. I. Siddiqui and S. A. Chaudhry, *Nigella sativa* plant-based nanocomposite-MnFe<sub>2</sub>O<sub>4</sub>/BC: an antibacterial material for water purification, *J. Clean. Prod.*, 2018, **200**, 996–1008.
- 104 M. A. Ibrahim, M. Z. Jaafar, M. A. M. Yusof, C. A. Shye and A. K. Idris, Influence of size and surface charge on the adsorption behaviour of silicon dioxide nanoparticles on sand particles, *Colloids Surf., A*, 2023, **674**, 131943.
- 105 T. Wollandt, S. Mangel, J. Kussmann, C. C. Leon, A. Scavuzzo, C. Ochsenfeld, K. Kern and S. J. Jung, Charging and Electric Field Effects on Hydrogen Molecules Physisorbed on Graphene, *J. Phys. Chem. C*, 2023, **127**, 4326–4333.
- 106 E. Allahkarami, A. D. Monfared, L. F. O. Silva and G. L. Dotto, Toward a mechanistic understanding of adsorption behavior of phenol onto a novel activated carbon composite, *Sci. Rep.*, 2023, **13**, 1–16.
- 107 O. Sahu and N. Singh, Significance of bioadsorption process on textile industry wastewater, *The Impact and Prospects of Green Chemistry for Textile Technology*, 2018, pp. 367–416.
- 108 S. Azizian and S. Eris, Adsorption isotherms and kinetics, *Interface Sci. Technol.*, 2021, **33**, 445–509.
- 109 N. Ayawei, A. N. Ebelegi and D. Wankasi, Modelling and Interpretation of Adsorption Isotherms, *J. Chem.*, 2017, **1**, 3039817.



- 110 P. Pourhakkak, A. Taghizadeh, M. Taghizadeh, M. Ghaedi and S. Haghdoost, Fundamentals of adsorption technology, *Interface Sci. Technol.*, 2021, **33**, 1–70.
- 111 K. H. Chu, Revisiting the Temkin Isotherm: Dimensional Inconsistency and Approximate Forms, *Ind. Eng. Chem. Res.*, 2021, **60**, 13140–13147.
- 112 Y. Liu, Y. Xiong, P. Xu, Y. Pang and C. Du, Enhancement of Pb (II) adsorption by boron doped ordered mesoporous carbon: Isotherm and kinetics modeling, *Sci. Total Environ.*, 2020, **708**, 134918.
- 113 N. Abbasi, S. A. Khan and T. A. Khan, Statistically optimised sequestration of mefenamic acid from polluted water by acacia gum phthalate/pectin hydrogel: a novel multifunctional adsorbent material synthesised via microwave-assisted process, *Chem. Eng. J.*, 2023, **466**, 143296.
- 114 H. K. Agbovi and L. D. Wilson, Adsorption processes in biopolymer systems: fundamentals to practical applications, *Natural Polymers-Based Green Adsorbents for Water Treatment*, 2021, pp. 1–51.
- 115 Y. Liu, New insights into pseudo-second-order kinetic equation for adsorption, *Colloids Surf., A*, 2008, **320**, 275–278.
- 116 S. A. Chaudhry, Z. Zaidi and S. I. Siddiqui, Isotherm, kinetic and thermodynamics of arsenic adsorption onto Iron-Zirconium Binary Oxide-Coated Sand (IZBOCS): modelling and process optimization, *J. Mol. Liq.*, 2017, **229**, 230–240.
- 117 J. Wang and X. Guo, Adsorption kinetic models: physical meanings, applications, and solving methods, *J. Hazard. Mater.*, 2020, **390**, 122156.
- 118 S. Madan, R. Shaw, S. Tiwari and S. K. Tiwari, Adsorption dynamics of Congo red dye removal using ZnO functionalized high silica zeolitic particles, *Appl. Surf. Sci.*, 2019, **487**, 907–917.
- 119 F. Bessaha, N. Mahrez, K. Marouf-Khelifa, A. Çoruh and A. Khelifa, Removal of Congo red by thermally and chemically modified halloysite: equilibrium, FTIR spectroscopy, and mechanism studies, *Int. J. Environ. Sci. Technol.*, 2019, **16**, 4253–4260.
- 120 Z. Zaidi, A. Manchanda, A. Sharma, Shehnaz, A. Choudhry, M. Sajid, S. A. Khan, A. Khan and S. A. Chaudhry, Adsorptive removal of Methylene blue using fruit waste activated carbon and its binary metal oxide nanocomposite, *Chem. Eng. J. Adv.*, 2023, **16**, 100571.
- 121 S. Sircar, Adsorbate mass transfer into porous adsorbents – a practical viewpoint, *Sep. Purif. Technol.*, 2018, **192**, 383–400.
- 122 W. J. Weber Jr and J. C. Morris, Kinetics of Adsorption on Carbon from Solution, *J. Sanit. Eng. Div.*, 1963, **89**, 31–59.
- 123 A. W. M. Ip, J. P. Barford and G. McKay, A comparative study on the kinetics and mechanisms of removal of Reactive Black 5 by adsorption onto activated carbons and bone char, *Chem. Eng. J.*, 2010, **157**, 434–442.
- 124 L. Ai, M. Li and L. Li, Adsorption of Methylene Blue from Aqueous Solution with Activated Carbon/Cobalt Ferrite/Alginate Composite Beads: Kinetics, Isotherms, and Thermodynamics, *J. Chem. Eng. Data*, 2011, **56**, 3475–3483.
- 125 M. Afkari, S. M. Masoudpanah, M. Hasheminasari and S. Alamolhoda, Effects of iron oxide contents on photocatalytic performance of nanocomposites based on g-C<sub>3</sub>N<sub>4</sub>, *Sci. Rep.*, 2023, **13**, 1–11.
- 126 C. Li, S. He, H. Mo, X. Xu, P. Yang and M. Liu, Recent developments of iron oxide-based photocatalysts in water treatment technology: a review, *Environ. Sci.*, 2025, **11**, 1369–1385.
- 127 M. Danish, M. S. Athar, I. Ahmad, M. Z. A. Warshagha, Z. Rasool and M. Muneer, Highly efficient and stable Fe<sub>2</sub>O<sub>3</sub>/g-C<sub>3</sub>N<sub>4</sub>/GO nanocomposite with Z-scheme electron transfer pathway: Role of photocatalytic activity and adsorption isotherm of organic pollutants in wastewater, *Appl. Surf. Sci.*, 2022, **604**, 154604.
- 128 S. Demirci, M. Yurddaskal, T. Dikici and C. Sarıoğlu, Fabrication and characterization of novel iodine doped hollow and mesoporous hematite (Fe<sub>2</sub>O<sub>3</sub>) particles derived from sol-gel method and their photocatalytic performances, *J. Hazard. Mater.*, 2018, **345**, 27–37.
- 129 C. N. C. Hitam and A. A. Jalil, A review on exploration of Fe<sub>2</sub>O<sub>3</sub> photocatalyst towards degradation of dyes and organic contaminants, *J. Environ. Manage.*, 2020, **258**, 110050.
- 130 A. Halfadji, A. Chougui, R. Djeradi, F. Z. Ouabad, H. Aoudia and S. Rajendrachari, TiO<sub>2</sub>-Decorated by Nano-γ-Fe<sub>2</sub>O<sub>3</sub> as a Catalyst for Efficient Photocatalytic Degradation of Orange G Dye under Eco-friendly White LED Irradiation, *ACS Omega*, 2023, **8**, 39907–39916.
- 131 E. D'Souza, A. B. Fulke, N. Mulani, A. Ram, M. Asodekar, N. Narkhede and S. N. Gajbhiye, Decolorization of Congo red mediated by marine *Alcaligenes* species isolated from Indian West coast sediments, *Environ. Earth Sci.*, 2017, **76**, 1–13.
- 132 B. S. Goud, H. L. Cha, G. Koyyada and J. H. Kim, Augmented Biodegradation of Textile Azo Dye Effluents by Plant Endophytes: A Sustainable, Eco-Friendly Alternative, *Curr. Microbiol.*, 2020, **77**, 3240–3255.
- 133 M. A. Sayed, A. Mohamed, S. A. Ahmed, A. M. El-Sherbeeney, W. Al Zoubi and M. R. Abukhadra, Enhanced photocatalytic degradation of Congo red dye into safe end-products over ZnO@polyaniline/coal composite as low cost catalyst under visible light: pathways and ecotoxicity, *J. Photochem. Photobiol., A*, 2024, **456**, 115843.
- 134 M. Thomas, G. A. Naikoo, M. U. D. Sheikh, M. Bano and F. Khan, Effective photocatalytic degradation of Congo red dye using alginate/carboxymethyl cellulose/TiO<sub>2</sub> nanocomposite hydrogel under direct sunlight irradiation, *J. Photochem. Photobiol., A*, 2016, **327**, 33–43.
- 135 B. Li, X. Zhao, Y. Huang, X. Lu, H. Jia and M. Li, Dual Z-scheme BiOI/Bi<sub>2</sub>S<sub>3</sub>/MgIn<sub>2</sub>S<sub>4</sub> composite photocatalyst for effective photocatalytic degradation of Congo red, *Environ. Sci. Pollut. Res. Int.*, 2023, **30**, 122537–122549.
- 136 G. He, Y. Li, W. Ji, Y. Hou, T. Zhu, Y. Chen, L. Yin and R. Liu, Highly efficient removal of Congo red from



- wastewater using biogenic vaterite: performance and mechanistic insights, *Surf. Interfaces*, 2025, **62**, 106270.
- 137 C. Fei, C. Chen, H. Zhang, A. Liu, D. Ju, X. Yang, F. Wang, M. Xia and P. Huang, The effective removal of Congo red dye via chitosan-layered double hydroxide composite and the deep insight into mechanism, *J. Ind. Eng. Chem.*, 2024, **135**, 143–153.
- 138 H. Kim, C. Park, N. Choi and K. Cho, Congo red dye degradation using Fe-containing mineral as a reactive material derived from waste foundry dust, *Environ. Sci. Pollut. Res.*, 2024, **31**, 28443–28453.
- 139 L. G. Devi, S. G. Kumar, K. M. Reddy and C. Munikrishnappa, Effect of various inorganic anions on the degradation of Congo Red, a di azo dye, by the photo-assisted fenton process using zero-valent metallic iron as a catalyst, *Desalination Water Treat.*, 2009, **4**, 294–305.
- 140 J. O. Ighalo, F. O. Omoarukhe, V. E. Ojukwu, K. O. Iwuozor and C. A. Igwegbe, Cost of adsorbent preparation and usage in wastewater treatment: a review, *Cleaner Chem. Eng.*, 2022, **3**, 100042.
- 141 Z. Sheerazi, I. Ahmad, S. A. Chaudhry, A. H. Sheikh and T. A. Khan, Green synthesis of a nicotinamide-functionalized cobalt ferrite nano-adsorbent for aqueous phase removal of some virulent dyes: evaluation of adsorption isotherms, kinetics, and mechanisms, *New J. Chem.*, 2025, **49**, 14590–14604.

